Identification of pharmacological inducers of a reversible hypometabolic state for whole organ preservation

Megan M. Sperry[1,2], Berenice Charrez[1], Haleh Fotowat[1], Erica Gardner[1], Kanoelani Pilobello[1], Zohreh Izadifar[1], Tiffany Lin[1], Abigail Kuelker[1], Sahith Kaki[1], Michael Lewandowski[1], Shanda Lightbown[1], Ramses Martinez[1], Susan Marquez[1], Joel Moore[1], Maria Plaza-Oliver[1], Adama M. Sesay[1], Kostyantyn Shcherbina[1], Katherine Sheehan[1], Takako Takeda[1], Daniela Del Campo[1], Kristina Andrijauskaite[3], Exal Cisneros[3], Riley Lopez[3], Isabella Cano[3], Zachary Maxwell[3], Israel Jessop[3], Rafael J. Veraza[3], Leon Bunegin[3], Thomas J. Percival[4], Jaclyn Yracheta[4], Jorge Pena[4], Diandra Wood[4], Zachary Homas[4], Cody Hinshaw[4], Jen Cox-Hinshaw[4], Olivia G. Parry[4], Justin J. Sleeter[4], Erik K. Weitzel[4], Michael Levin[1,2,5], Michael Super[1], Richard Novak[1], Donald E. Ingber[1,6,7]*

[1]Wyss Institute for Biologically Inspired Engineering at Harvard University
[2]Department of Biology, Tufts University
[3]Vascular Perfusion Solutions, Inc
[4]RESTOR™, 59th Medical Wing, JBSA, Lackland AFB
[5]Allen Center, Tufts University
[6]Vascular Biology Program & Department of Surgery, Boston Children's Hospital and Harvard Medical School
[7]Harvard John A. Paulson School of Engineering and Applied Sciences
*Corresponding author: Donald E. Ingber, MD, PhD, Wyss Institute at Harvard University, 201 Brookline Ave., Suite 401, Boston, MA, 02215 USA (Em: don.ingber@wyss.harvard.edu)

ABSTRACT

Drugs that induce reversible slowing of metabolic and physiological processes would have great value for organ preservation, especially for organs with high

susceptibility to hypoxia-reperfusion injury, such as the heart. Using whole-organism screening of metabolism, mobility, and development in *Xenopus*, we identified an existing drug, SNC80, that rapidly and reversibly slows biochemical and metabolic activities while preserving cell and tissue viability. Although SNC80 was developed as a delta opioid receptor activator, we discovered that its ability to slow metabolism is independent of its opioid modulating activity as a novel SNC80 analog (WB3) with almost 1,000 times less delta opioid receptor binding activity is equally active. Metabolic suppression was also achieved using SNC80 in microfluidic human organs-on-chips, as well as in explanted whole porcine hearts and limbs, demonstrating the cross-species relevance of this approach and potential clinical relevance for surgical transplantation. Pharmacological induction of physiological slowing in combination with organ perfusion transport systems may offer a new therapeutic approach for tissue and organ preservation for transplantation, trauma management, and enhancing patient survival in remote and low-resource locations.

Tissue and organ loss to trauma, disease, and physical injury account for a large proportion of human ailments and approximately $400 billion in annual medical burden.[1] The rapid and reversible slowing of metabolic and other physiological processes, here referred to as 'biostasis', can improve the survival of cells and organs for transplantation. This is currently accomplished clinically by lowering temperature and static cold storage is the standard of care for organ and tissue preservation; however, its long-term use can cause damage to the integrity of the graft.[1–3] Hypothermia also has been used to induce a state of biostasis clinically using *ex-vivo* machine perfusion technologies, for example, during cardiac transplant surgery. Combination of protective agents with perfusion and/or partial freezing approaches have extended preservation times in rat livers and whole pigs,[4,5] and neural modulation approaches have been successful at demonstrating central control of body temperature and general metabolic state.[6,7] However, both mechanical cooling and neural stimulation approaches are

55 challenging to implement in a trauma triage or resource-limited situations, which would be better
56 addressed by pharmaceutical interventions.

57 Several molecular strategies have been proposed to achieve metabolic suppression for
58 organ preservation, including modulating H_2S, AMPK, opioid receptors, microRNAs, HO-1, and
59 Nrf2.[8] H_2S exposure has been reported to induce a hypometabolic state (reduced metabolism
60 and body temperature) in a rodent model, although this was later found to be mediated in part
61 by a low baseline laboratory temperature.[9] The synthetic opioid peptide DADLE also can induce
62 hypometabolism and improve organ preservation via a delta opioid receptor (DOR) mechanism,
63 but with varied results.[10,11] Compounds that directly impact glycolysis and mitochondrial
64 respiration also have been considered for modulating organ metabolism, but many are acutely
65 toxic and not reversible, fail to protect tissues from ischemic injury, or lack drug-like properties.
66 Specifically, reduced functionality of the mitochondrial electron transport chain system without
67 the endogenous antioxidant and anti-inflammatory molecules released by hibernators can result
68 in the release of reactive oxygen species and cause tissue damage.[8]

69 Despite these efforts, there remains a large unmet need for improved tissue and organ
70 preservation approaches across multiple application areas. Thus, in the present study, we set
71 out to identify small molecules that could slow metabolism and mimic states normally induced
72 by hypothermia, hibernation, or torpor, which could be used for preservation of living cells,
73 tissues, and organs ex v*ivo*, and potentially *in vivo* as well. Specifically, we required this
74 biostasis approach to be rapidly inducible (< 1 hour) and safely reversible, with major tissue
75 functions returning to control levels within 24 hours.

76 Through survey of the literature, we identified drugs with unintended side effects, such
77 as lowering body temperature, which suggested they might have broad effects on metabolism.
78 Among these drugs was SNC80, a small molecule drug originally developed as a nonaddictive
79 pain reliever that acts independently of the mu-opioid pathway.[12] This drug caught our attention
80 because it has been shown to induce hypothermia and protect against the effects of spinal cord

81 ischemia in rodents.[12,13] To explore whether SNC80 had potential to broadly slow tissue
82 metabolism and physiology, we administered the drug to *Xenopus laevis* embryos and tadpoles,
83 which we and others have previously shown to be useful models for drug screening due to their
84 small size, extrauterine development, and skin permeability to small molecules.[14–17] The
85 Xenopus tadpoles were dosed at higher levels than dictated by SNC80's defined IC50 value,
86 with the goal of exploring the effects of SNC80 outside its known pain relief properties and
87 accentuating the drug's "off-target" effects, including hypometabolism.

88 **Demonstration of physiological slowing in *Xenopus***

89 We first assessed SNC80's impacts on mobility, metabolism, and heart activity in
90 *Xenopus*. Behavioral assessment in mobile tadpoles showed that 100 μM SNC80 slows
91 movement relative to vehicle-treated counterparts, reducing activity by approximately 50%
92 within 1 hour, which is rapidly reversible when the drug is removed (**Figure 1a**). SNC80 also
93 suppressed the rate of oxygen consumption to one-third of baseline within 3 hours of treatment
94 (**Figure 1b**) and had extreme suppressive, but fully reversible, effects on heart rate after only 1
95 hour of exposure (**Figure 1c**)**.** Oxygen consumption was reduced in immobile *Xenopus* embryos
96 treated with SNC80 as well (**Figure S1a**), suggesting that its metabolism-suppressing effects
97 are independent of the slowed movement observed in mobile tadpoles.

98 Using *in situ* Matrix-Assisted-Laser Desorption/Ionization-Time of Flight Mass
99 Spectrometry Imaging (MALDI-ToF MSI), we assessed and visualized the biodistribution of
100 SNC80 in the *Xenopus* tadpole. SNC80 was detected within 1 hour of treatment and it appeared
101 in a punctate distribution in the gastrointestinal (GI) tract, gill region and skeletal muscle
102 (**Figures 2a,b**), suggesting full-body delivery of the drug. Past lipidomic studies of hibernating
103 mammals demonstrated the importance of lipid molecules for thermal adaptation during
104 hibernation with significant alterations of lipidomic profiles being observed in liver, plasma, brain,
105 skeletal muscle and cardiac muscle during torpor as compared to the animal's active state.[18,19]
106 Similarly, MALDI-ToF MSI analysis revealed significantly higher levels of acylcarnitine and

107 cholesterol ester in SNC80-treated groups in both skeletal muscle and brain (**Figure 2c**).
108 Increased levels of long chain acylcarnitine associated with enhanced mitochondrial fatty acid
109 oxidation are observed during fasting as well as in hibernating brown bears,[20,21] and cholesterol
110 ester levels increase in hibernating ground squirrels.[22] While the increased acylcarnitine and
111 cholesterol ester levels in brain suggest a shift towards beta oxidation of fatty acids, they also
112 have been implicated in other pathways including antioxidant activity and neurotransmission.[23,24]
113 Having confirmed that SNC80 induces slowing of multiple physiological parameters in
114 the whole *Xenopus* organism, we then set out to explore the molecular basis for these effects.
115 As SNC80 is a known DOR agonist,[12,13] we next evaluated whether its effects could be
116 mediated by delta opioids. However, when we tested the DOR antagonist, naltrindole (NTI), at
117 double the concentration (200 μM), it did not block the hypometabolic effects of SNC80 (**Figure**
118 **2d**), suggesting that SNC80 modulates metabolism independent of DOR activation.

119 **Attenuating the delta opioid activity of SNC80**

120 To further test if the physiological slowing effects of SNC80 are independent of DOR
121 activation, we used a medicinal chemistry approach to explore whether we could separate its
122 metabolism slowing and DOR activities. Toward this end, we designed molecular entities void of
123 the distal basic nitrogen (N-ally group within SNC80), which we hypothesized was a critical DOR
124 pharmacophore. This effort led to the development of a novel morpholino compound, WB3
125 (**Figure 3a** & **Supplemental Synthesis Description**), which was synthesized and subsequently
126 tested for DOR binding activity using a radioligand binding assay and non-linear fitting for
127 specific binding to calculate the Hill Slope and IC50 value. A specific binding curve could not be
128 fit for SNC80 due to its high affinity and therefore its IC50 is <4.6 nM, whereas WB3 exhibited
129 an IC50 of 3,470 nM (**Figure 3b**), suggesting almost 1,000 times less DOR binding activity for
130 WB3 compared to SNC80. Subsequently, we screened WB3 in the *Xenopus* swimming and
131 heart rate assays and found that the analog retains physiological slowing properties *in vivo*
132 despite lacking delta opioid activity (**Figure 3c,d**). In fact, we observed more potent and rapid

133 effects on swimming with exposure to WB3 compared to SNC80, suggesting that the non-opioid
134 properties of SNC80 may be primarily responsible for its observed physiological effects.

135 **Enhanced preservation of whole pig hearts and limbs perfused *ex vivo***

136 Based on these intriguing findings with human Organ Chips and *Xenopus* tadpoles, we
137 set out to explore the potential clinical value of SNC80. Cardiac transplant is the gold standard
138 for treating end-stage heart failure; however, it is hindered by donor shortage, limited cardiac
139 graft preservation time, and lack of optimal organ preservation conditions. Currently, hearts are
140 allocated to patients located within 4 hours of organ removal from the donor. Thus, to explore
141 the potential utility of biostasis induction to lengthen the time between organ donation and
142 recipient surgery through pharmacological induction of a hypometabolic state, we perfused
143 surgically explanted whole porcine hearts with SNC80 using a portable, oxygenated perfusion
144 preservation device (VP.S ENCORE®) at subnormothermic temperatures (20-23°C). Prior work
145 has demonstrated that the VP.S ENCORE® enhances cardiac viability over standard of care-
146 static cold storage and hearts perfused in this device for 4 hours demonstrate similar cardiac
147 function to a healthy heart in both preclinical animal models and human deceased donor
148 hearts.[25,26]

149 We investigated the application of a biostasis inducer for preservation of the heart during
150 6 hours of perfusion in the VP.S ENCORE® device. Importantly, with SNC80 treatment, we
151 observed a rapid decline in the heart's oxygen consumption to < 50% of that observed in hearts
152 exposed to the vehicle control, which was sustained over the 6-hour preservation period (**Figure**
153 **4a**). After preservation, hearts were removed from the VP.S ENCORE® and placed in a
154 Langendorff system for reperfusion and evaluation of oxygen consumption and cardiac
155 contractility. This system assesses the left ventricular dP/dT without preload and afterload,
156 thereby allowing the evaluation of the intrinsic contractility of the left ventricle. After 30 minutes
157 of reperfusion and before defibrillation, SNC80-treated hearts had a lower oxygen consumption
158 level than vehicle treated hearts (2.39 ± 1.23 versus 4.28 ± 2.48 ml/min/100g, respectively, at

159 the 30-minute timepoint) (**Figure 4b)** that recovered to normal levels after defibrillation and with
160 increases in temperature (2.49 ± 0.53 and 2.35 ± 0.31 ml/min/100g, respectively, at 60 minutes
161 post-defibrillation) (**Figure 4c**). No evidence of substantial change in left ventricle (LV)
162 contractility or relaxation were detected in SNC80-exposed hearts, either before or after they
163 were defibrillated and exposed to epinephrine (**Figure 4d**).

164 Gene expression analysis of heart biopsy samples showed significant reduction of
165 markers of inflammation (IL-6, IL-8, TNFα), hypoxia (Hif1α), and cell death (TP53, BCL2) in
166 SNC80-treated hearts when compared to vehicle control hearts (**Figure 4e**), and no changes in
167 the mitochondrial ATP synthase marker, ATP5MC3, were observed. Histopathological
168 evaluation showed retention of normal muscle morphology (**Figure 4f**) without signs of tissue
169 edema immediately after perfusion in the VP.S ENCORE®. In some hearts treated with SNC80
170 greater waviness of muscle fibers was observed, possibly indicating a state of muscle
171 contraction.

172 Electrocardiogram (ECG) data revealed that both vehicle and SNC80-treated hearts
173 exhibited irregular beating after perfusion and prior to defibrillation. After defibrillation with
174 epinephrine, the P and QRS waveforms were visible in ECGs from 3 of 4 SNC80-treated hearts
175 (**Table S1**), suggesting that those hearts regain atrial and ventricular polarization. The pulse
176 rates of SNC80-treated hearts were at or near normal range for porcine hearts (70-120
177 beats/min) after defibrillation. Vehicle-treated hearts exhibited tachycardia following
178 defibrillation, with all exhibiting pulse rates above the normal range for porcine hearts.

179 We also tested organ preservation in porcine limbs, where prolonged ischemia after
180 amputation rapidly decreases the viability of skeletal muscle. Current preservation methods limit
181 the success of limb reimplantation due to complications from rhabdomyolysis, necrosis, and
182 reperfusion injury.[27] Again, we found that the relative metabolic rate measured during 3 hours of
183 SNC80 exposure was significantly lower compared to vehicle-treated limbs (**Figure S2a**).
184 Histopathological evaluation also showed retention of normal muscle morphology with no

185 apparent changes in muscle bundle area (**Figure S2b**) or glycogen content (**Figure S2c**)
186 suggesting that the tissue's potential for ATP synthesis was not compromised after SNC80
187 administration, although an increase in intercellular spacing was observed (**Figure S2d**). We did
188 not observe full recovery of O_2 uptake at the 3-hour time point analyzed in this study (**Figure**
189 **S2c**); however, the porcine limb contains a large amount of fat tissue that may be acting as a
190 depot for the highly lipophilic SNC80, thereby leading to extended stasis under these conditions.

191 **Elucidating potential SNC80 targets and pathways**

192 To gain insight into the molecular basis of SNC80's hypometabolic and other
193 physiological effects, we used thermal proteome profiling (TPP) to assess drug-protein binding
194 and thereby identify previously unknown molecular targets of SNC80 that might be critical for its
195 metabolism slowing activity. TPP of SNC80-treated *Xenopus* tissues revealed 19 direct and
196 indirect binding targets (**Table 1**), including proteins involved in transmembrane transport,
197 mitochondrion activity, and metabolic processes. Two potentially interesting binding targets of
198 SNC80 are the excitatory amino acid transporter 1 (EAAT1; also known as SLC1A3) and the
199 Na^+/Ca^{2+} exchanger 1 (NCX1; also known as SLC8A1), both of which have been identified in
200 cardiac tissue.[28,29] In addition to their individual functions, mitochondrial ATP production has
201 been previously reported to be stimulated through intermolecular interactions between EAATs
202 and NCXs in neurons.[30] If this complex is also present in cardiac tissue, inhibition of EAAT and
203 NCX1 could reduce cellular ATP levels,[31] and thereby play a role in slowing metabolism.
204 Specifically, the blockade of Na^+/Ca^{2+} exchange via interference with EAAT1-NCX1 interactions
205 could prevent the influx of calcium into the mitochondria that is necessary for calcium-sensitive
206 mitochondrial dehydrogenases that fuel ATP synthesis.[32] However, the mitochondrial variant of
207 NCX1 (NCLX) was not included in the *Xenopus* protein library used for TPP analysis so could
208 not be fully evaluated in this study. TPP also identified two additional SNC80-binding proteins
209 located within the mitochondrion: TOMM40 and COX6C. TOMM40 is a translocase located in
210 the outer membrane of the mitochondria that has been implicated in tissue protective effects

211 against late-onset Alzheimer disease[33] and COX6C is the terminal enzyme of the mitochondrial
212 respiratory chain, catalyzing the electron transfer from reduced cytochrome c to oxygen.
213 In addition to interaction with mitochondrial proteins, we detected binding between
214 SNC80 and enzymes involved in other metabolic processes, including alpha-L-fucosidase 2
215 (FUCA2), cysteine conjugate beta-lyase (CCBL1), retinoid isomerohydrolase (RPE65), and
216 acyl-CoA Oxidase 3 (ACOX3). SNC80 also binds to multiple membrane-spanning proteins,
217 including vacuole membrane protein 1 (VMP1) and ABCB1, an ATP-dependent translocase, in
218 addition to NCX1 and EAAT1. The drug also bound to two proteins of the immune system,
219 histocompatibility minor 13 (HM13) and pentraxin 3 (PTX3), as well as two cytoskeletal proteins,
220 calmodulin regulated spectrin associated protein family member 2 (CAMSAP2) and integrin
221 subunit alpha 7 (ITGA7). Interestingly, SNC80 also bound to four ribosomal proteins, RPL4,
222 RPL27A, RPS25, and RRP9, which are frequent targets of antibiotic and antiviral drugs.
223 Collectively, these data suggest that induction of physiological slowing by SNC80 may involve
224 simultaneous modulation of multiple pathways, with critical mechanisms involving mitochondria,
225 membrane-spanning transporters, and possibly other metabolic processes as well.
226 **Metabolic suppression in human Organ Chips**
227 To explore whether this drug also induces a state of biostasis in human cells and tissues, as
228 well as non-cardiac cells, we tested SNC80 in human organ-on-a-chip (Organ Chip) microfluidic
229 culture devices that reconstitute tissue-tissue interfaces and human organ-level physiology with
230 high fidelity in vitro.[34] The Organ Chip models reconstitute a tissue-tissue interface between
231 organ-specific epithelium and endothelium across a porous extracellular matrix-coated
232 membrane within a two-channel microfluidic device, and hence allow tissue-tissue cross talk
233 observed in vivo that is not normally present in studies with cultured cells, as previously
234 described.[35,36] In this study, we used a Gut Chip lined by Caco-2 intestinal epithelial cells
235 interfaced with HUVECs and a Liver Chip containing Huh7 liver epithelial cells interfaced with
236 LSECs, respectively. However, we modified the Organ Chip design by integrating sensors that

237 allow for live monitoring of oxygen (O_2) and transepithelial electrical resistance (TEER) (tissue
238 barrier function) (**Figure S3a**). Both Organ Chips were treated with SNC80 by flowing the drug
239 in medium for 2 days through the apical and basal channels of the chip, and then removing the
240 drug followed by 7 days of additional culture. We confirmed that the intestinal epithelial cells
241 underwent villus differentiation and accumulated mucus under these culture conditions (**Figure**
242 **S3b**), in addition to maintaining a low oxygen environment after 10-16 days of culture (**Figure**
243 **S3c**) as previously described.[35,36] The Liver Chips also produced albumin and urea at levels (5
244 and 135 µg/day/chip, respectively) (**Figure S3d,e**) that were similar to those measured in Organ
245 Chips lined by primary hepatocytes.[37,38]

246 These studies revealed that SNC80 treatment reduced the respiratory (oxygen
247 utilization) rate in the Gut Chip, resulting in an almost 6-fold increase in extracellular oxygen
248 levels after 48 hours, which then progressively returned to baseline levels during the 7-day
249 washout period (**Figure S4a**). Similar results were obtained with the more highly metabolic
250 Liver Chip with SNC80 inducing higher levels of extracellular oxygen compared to control chips
251 and this again reversed after drug washout (**Figure S4a**). Importantly, the tissues in both the
252 human Organ Chips remained healthy after 2 days treatment with SNC80 as there was no
253 significant change in barrier function (**Figures S5a,b**), cell growth (**Figure S3**), or cytotoxicity
254 (**Figures S5c,d**). Similar to the data observed in cell cultures, ATP/ADP ratio in Liver Chips was
255 significantly decreased after 24 and 48h of SNC80 treatment compared to the vehicle control
256 chips. However, ATP/ADP ratio measurements between SNC80 and vehicle control were not
257 significantly different after washout of the drug, indicating that Liver Chip tissues recover their
258 normal metabolic function up to 4 days after treatment (**Figure S4b**).

259 Collectively, these data suggest that treatment with SNC80 in these physiologically
260 relevant human cells and tissues cultured on-chip in an organ-relevant context resulted in a
261 drop in respiration, with no switch towards glycolysis or reductive carboxylation, since the levels
262 of lactate (**Figure S5e,f**) and glutamate remained unchanged in both chips (**Figure S5g,h**).

263 Thus, in this organ-like microenvironment, the tissues decrease their total ATP production in
264 presence of SNC80, which is accompanied by a global slowing of metabolism.
265
266 **Discussion**
267 Here we report the discovery that the small molecule drug, SNC80, and its analog WB3,
268 are capable of slowing of multiple physiological processes, and thereby inducing a
269 hypometabolic state without external cooling. Although there is extensive clinical experience
270 using hypothermia to cryopreserve organs during surgery (e.g., cardiac bypass) and for donor
271 transplants, comparatively little work has been done in the area of molecular induction of
272 biostasis without external cooling. We found that SNC80 reversibly suppressed metabolism
273 across multiple cell and tissue types, as well as different species and experimental models, at
274 their basal temperatures, suggesting that this approach could be appropriate for preservation of
275 a variety of cells, tissues, and organs. Critically, integrating this small molecule drug in a
276 commercial organ preservation system with whole explanted pig hearts demonstrated potential
277 for near-term translation and impact of this approach for applications relating to organ
278 preservation and surgical transplantation.
279 Initially developed as a nonaddictive pain reliever, SNC80 was previously shown to
280 induce hypothermia and protect against the effects of spinal cord ischemia in rodents,[12,13] but its
281 broad effects on metabolism were not known. In the present study, treatment with SNC80
282 slowed swimming movement and reduced oxygen consumption rates in a reversible manner in
283 *Xenopus* tadpoles, and it lowered the metabolic rate in non-mobile *Xenopus* embryos as well.
284 Importantly, SNC80 displayed similar metabolism suppressing activities that were reversible in
285 physiologically relevant human Organ Chip microfluidic devices that reconstitute organ-level
286 structures and functions in vitro. These data suggested that induction of a hypometabolic state
287 by this small molecular drug could potentially provide a new paradigm to prolong organ
288 preservation. Indeed, when we perfused explanted porcine hearts and limbs with SNC80, we

289 experimentally confirmed that this biostasis agent can slow metabolism in a whole complex
290 living organs, providing direct support for its potential integration into commercial organ
291 preservation devices that strive to extend the viability of human organs for surgical
292 transplantation.

293 SNC80 is defined as a highly selective non-peptide DOR agonist drug and other DOR
294 agonists, such as the enkephalin DADLE, have been shown to reduce metabolic demand and
295 protect against oxidative stress, thereby decreasing injury and apoptosis in perfused
296 organs.[8,10,11] Prior studies of DADLE found that the DOR pathway was required to alter
297 metabolism and provide protective effects, however, we found that SNC80 suppresses
298 metabolism via a mechanism that is independent of its DOR modulating activity. Instead, we
299 found that SNC80 interacts with multiple proteins involved in transmembrane transport,
300 mitochondrion activity, and metabolic processes. Interestingly, one of the identified targets,
301 NCX1, has been previously implicated in control of temperature compensation and autonomous
302 oscillation,[39] suggesting that it plays a key role in the regulation of biochemical reaction speed,
303 cell cycle, and other forms of biological timing, such as circadian rhythm. In addition to its
304 effects on tissues of the nervous system, multiple drugs that target Na^+/Ca^{2+} exchange by NCX,
305 such as the KBR family of drugs, were developed for the treatment of ischemia, reperfusion
306 injury, and heart arrhythmias.[40] In rats, pre-ischemic or post-ischemic treatments with KBR
307 compounds improved recovery of ventricular pump function and reduced reoxygenation-induced
308 injury as measured the reduced release of intracellular components (e.g., lactate
309 dehydrogenase).[40,41] Our results suggest that SNC80 could be acting on the NCX1
310 transmembrane protein and/or NCX1/EAAT1 pathway may result at least in part from induction
311 of a hypometabolic state.[45] Of the tissues impacted by SNC80, the observed effects were most
312 profound on *Xenopus* tadpole heart function and porcine hearts. SNC80 and other opioids have
313 been shown to decrease cardiac inotropy and contractility,[42,43] and prior work has demonstrated
314 that decreases in cardiac inotropy and contractility by opioid agonists may be mediated by

315 opioid receptor-*independent* actions of these drugs.[43] Substantial slowing of heart rate by WB3,
316 which exhibits approximately 1,000 times less delta opioid activity than SNC80, further supports
317 this claim. Similar to our findings by TPP, other investigators identified *non-opioid* receptor-
318 mediated actions of these compounds on ion channel function.[43] Changes in contractility were
319 not observed immediately after perfusion with SNC80 in porcine hearts tested here, likely
320 because the SNC80 was washed out of the tissue before contractility was measured; however,
321 future work should continue to monitor these parameters, especially at later time points.
322 Although bradycardia likely contributes to the hypometabolism observed in both systems, we
323 also see reduced metabolic rates in systems lacking cardiac cells, and thus the hypometabolic
324 activity of SNC80 we observed is not completely cardiac-specific.

325 The *Xenopus* and perfused porcine heart systems may be particularly amenable to
326 extreme slowing of cardiac output because these live tissues are surrounded by well-
327 oxygenated medium during treatment, potentially avoiding tissue injury sometimes associated
328 with hypometabolic states. However, the assumption that high oxygen content in the perfusate
329 completely precludes ischemia may not be valid. Assuming adequate flushing during recovery,
330 local vasospasm or a fat micro embolism occurring during perfusion could restrict perfusion flow
331 thereby inducing a localized hypoxic state and HIF1α expression in the tissue. SNC80 may be
332 acting in a vasodilatory capacity, thereby facilitating oxygen delivery and suppressing HIF1α
333 expression. In addition, although HIF1α is primarily known for its role in response to hypoxia, it
334 has some oxygen-independent functions and can be induced by factors other than oxygen
335 levels, such as growth factors and cytokines, which can activate its transcriptional activity even
336 under normoxic conditions. In these cases, HIF1α can regulate genes involved in cell
337 proliferation, metabolism, inflammation, and other cellular processes. Therefore, observation of
338 suppressed HIF1α, as well as the reduction of multiple inflammatory and cell death markers, in
339 the treated porcine cardiac tissue suggests a protective effect of SNC80.

340 Before considering broader applications of SNC80 or any of its analogs, such as whole-
341 body infusion during trauma or infection, it will be critical to consider impacts of this drug not
342 only on the heart but other organ systems as well. In particular, our *Xenopus* data suggest that
343 there could be substantial uptake of SNC80 in the brain, thus potentially impacting tissues of the
344 central nervous system. Therefore, future work should characterize cognitive recovery in
345 organisms receiving systemic delivery of stasis inducers. In addition, whole-body infusion
346 applications may require further pharmaceutical development, including chemical modifications
347 to SNC80 and development of targeted delivery methods to ensure clinical safety.
348 In summary, our findings demonstrate that the small molecule drugs SNC80 and WB3
349 can be used as a biostasis inducer to produce a hypometabolic state, which can provide
350 potential therapeutic value for clinical applications, such as enhanced preservation of organs.
351 The use of a biostatic compound in combination with a self-contained transport system could
352 potentially increase organ viability for sustained times *ex vivo*, thus helping to advance organ
353 and tissue preservation for surgical transplantation. The ability to induce a reversable
354 hypometabolic, suspended animation-type state rapidly through injection at the point-of-care
355 also could enable new therapeutic approaches to slow the detrimental effects of trauma and
356 acute infection, thereby increasing patient survival in military settings and space exploration, as
357 well as in civilian health emergency operations. It also may be possible to use this biostasis
358 approach to slow metabolic activities in the brain in cases of stroke or traumatic brain injury,
359 indications for which current treatments are severely limited.

360 ## Methods

361 ***Xenopus* model.** *Xenopus* embryos were fertilized at Tufts University using procedures
362 reviewed and approved by the Tufts University Institutional Animal Care and Use Committee
363 regulations and transferred to the Wyss Institute. *Xenopus* embryos and tadpoles were housed
364 at 18°C with a 12/12 h light/dark cycle in 0.1X Marc's Modified Ringer's (MMR) medium. All
365 animal experiments and procedures were reviewed and approved by the Harvard Medical
366 School (HMS) Institutional Animal Care and Use Committee regulations.

367 Drugs used in the *Xenopus* studies were dissolved in DMSO to a stock concentration of
368 10 mM and diluted to their final concentrations with a 1% DMSO concentration or less. Media
369 with dosed compound were made fresh and screening was performed in tadpoles at Stages 46-
370 50. The activity of free-swimming tadpoles during and after exposure to drugs were recorded in
371 60 mm dishes using a SONY Alpha a6100 camera with 16 mm objective (Sony Corporation,
372 Tokyo, Japan) against an illuminated background. Mobility was quantified in Matlab (Mathworks,
373 Natick, MA) by mapping differences between frames to a movement index (0 – 1), with 0
374 indicating no movement and 1 indicating maximal movement. Oxygen consumption was
375 measured during *Xenopus* exposure to drugs as a proxy for whole-organism metabolism using
376 the Firesting Optical Oxygen Meter and the Pyro Oxygen Logger software (version 3.317)
377 (Pyroscience GmbH, Aachen, Germany). Oxygen consumption for *Xenopus* embryos was
378 measured using the OxoPlate (PreSens Precision Sensing GmbH, Regensburg, Germany).
379 Oxygen consumption rate for each sample was measured using a linear fit to the oxygen
380 consumption curves in Prism (GraphPad, San Diego, CA). Heart rate was measured by
381 microscopy imaging in *Xenopus* following 1, 2, 4, or 8 hours of drug exposure. Vehicle and
382 drug-treated groups were briefly incubated in 0.01% tricaine (Syndel, Ferndale, WA) to minimize
383 tadpole movement during heart imaging. Videos of heart function were acquired using a ZEISS
384 Axio Zoom.V16 microscope and ZEN BLUE Microscopy software (version 3.1) (Carl Zeiss AG,

385 Oberkochen, Germany) at a rate of 1 frame/100 ms. Heart beats were counted automatically
386 using a custom code in Python. At the completion of experiments, *Xenopus* were euthanized by
387 immersion in 0.2% tricaine for 30 minutes, followed by fixation or bleaching and disposal.
388 **MALDI-ToF.** Tadpoles were embedded in gelatin (0.11 g/mL) and stored in -80C.
389 Embedded tadpoles were sectioned into 16 um-thick slices using a Leica CM1850 (Leica
390 Microsystems, Wetzlar, Germany) onto indium tin oxide (ITO)-coated glass slides (Bruker
391 Daltonics, Billerica, MA) and immediately placed in a vacuum desiccator before matrix
392 application (N=5 tadpoles per condition; N=3 sections/slide). Experiments were duplicated to
393 confirm the reproducibility. The matrix solution was composed of 2,4 Dihydroxybenzoic acid
394 (40mg/mL) in 0.1% formic acid, methanol/water (1:1 v/v) and was made fresh for each
395 application. The HTX-sprayer nebulizer (HTX Technologies, Carrboro, NC, USA) was used to
396 apply the matrix at 80°C at 24 passes over the sample, at a flow rate of 50μL/min, 10 psi
397 pressure and a track speed at 1,250 mm/min. Before imaging, SNC80 spotting with matrix and
398 *Xenopus* lysate was performed to determine the optimal matrix for the best S/N ratio and the
399 least ion suppression from *Xenopus* tissue and to identify which adducts were detectable for
400 each compound for imaging. *In situ* MALDI-ToF imaging was acquired using the rapifleX (Bruker
401 Daltonics, Billerica, MA), in positive ion mode at 1000 Hz in the mass range of 300-990 m/z. The
402 laser raster step spacing was set to 45 μm step size at 500 shots per pixel. External calibration
403 was performed using a red phosphorus slurry drop casted on a region of the ITO slide without
404 tissue. Preliminary processing of the data was performed using FlexAnalysis (Bruker Daltonics,
405 Billerica, MA). Images were normalized by the total ion count and baseline-corrected using Top
406 Hat algorithm with a _baseline width. After MALDI-ToF MSI acquisition, ITO slides were then
407 stained for H&E and imaged using the Cytation 5 (Agilent, Santa Clara, CA) and Epsilon
408 scanner at 3000 dpi to select regions of interest using the open-source program, Qupath.[44]
409 Mass selection windows and signal intensity analysis was conducted with SCiLS Lab (Bruker
410 Daltonics, Billerica, MA), where ions of interest, including SNC80, acylcarnitine and cholesterol

411 ester C18, were chosen with a width of ±0.25 Da. Reference peaks of target analytes were
412 based on previous MALDI-ToF work in Xenopus tissues from previous findings,[45] and during
413 spotting of target analytes with MALDI-ToF MS/MS. The mean signal intensity of the defined
414 regions of interest were obtained with each ion of interest.

415 **Radioligand binding assay.** To assess binding of WB3 to the delta opioid receptor, we
416 tested WB3 and SNC80 at 8-concentrations with 3-fold serial dilutions starting at 10 μM
417 (Reaction Biology, Malvern, PA). Binding of the tracer [3H]-DADLE (10 nM) was assessed in the
418 presence of each concentration of WB3 and SNC80 and the [3]-DADLE signal was fit to a dose-
419 response curve to quantify the Hill Slope and IC50 values.

420 **Thermal proteome profiling.** To identify drug-bound targets based on altered thermal
421 stability, *Xenopus* tadpoles were treated with either SNC80 or vehicle for 2 hours. *Xenopus*
422 were euthanized in 20X tricaine and then transferred back to their respective drug solutions to
423 ensure drug effect is not lost during heat treatment. *Xenopus* samples were incubated at 9
424 temperature points (30C, 35C, 40C, 44C, 48C, 52C, 56C, 60C, 65C) using a PCR machine (3
425 minutes heat time per condition, 3 tadpoles per condition) for both drug treated and vehicle
426 treated groups. After transfer to room temperature, liquid was aspirated from samples and
427 samples were snap frozen in liquid nitrogen. Samples were lysed in 100 μl of PBS + 0.4 % NP-
428 40 with 4 cycles of freeze/thaw. 11μl of each of the 9 temperatures were pooled in one tube and
429 samples were centrifuged at 13,000 RPM for 75 minutes, at 4C. Proteins were reduced and
430 alkylated with 10 mM DTT and 15 mM IAA for 15 minutes at 65C and 30 minutes at room
431 temperature, respectively. Proteins were then precipitated with 8 volumes of ice-cold acetone
432 and 1 volume of ice-cold methanol overnight. Digestion was carried for 4 hours in 50 mM Tris ph
433 8 + 0.75 mM Urea + 1μg trypsin/LysC at 37 Celcius with agitation. Another 1 μg of trypsin/LysC
434 was added and digestion was continued overnight. Peptides were purified by reversed phase
435 SPE and analyzed by LC-MS/MS (PhenoSwitch Bioscience, Sherbrooke, QC, Canada). LC-
436 MS/MS acquisition was performed with a ABSciex TripleTOF 6600 (ABSciex, Foster City, CA,

437 USA) equipped with an electrospray interface with a 25 µm iD capillary and coupled to an
438 Eksigent µUHPLC (Eksigent, Redwood City, CA, USA). Analyst TF 1.8 software was used to
439 control the instrument and for data processing and acquisition. Samples were acquired twice in
440 SWATH acquisition mode using gas phase fractionation. The source voltage was set to 5.5 kV
441 and maintained at 325C, curtain gas was set at 45 psi, gas one at 25 psi and gas two at 25 psi.
442 Separation was performed on a reversed phase Kinetex XB column 0.3 µm i.d., 2.6 µm
443 particles, 150mm long (Phenomenex) which was maintained at 60C. Samples were injected by
444 loop overfilling into a 5µL loop. For the 60 minutes LC gradient, the mobile phase consisted of
445 the following solvent A (0.2% v/v formic acid and 3% DMSO v/v in water) and solvent B (0.2%
446 v/v formic acid and 3% DMSO in EtOH) at a flow rate of 3 µL/min. GPF files for both acquisitions
447 were analyzed on a previously generated 3D ion library. Each GPF file was analyzed using 10
448 peptides per protein, 4 MS/MS transition per peptide, 12.5-minute RT window and 25 ppm XIC
449 width in Peakview (Sciex). The reported quantification for a protein is the sum of all the correctly
450 integrated peptides (FDR<0.05) in both GPF files.

451 **Human Cell Cultures:** Caco2 intestinal epithelial cells were grown in high glucose
452 (4.5g/L) DMEM (Gibco), 10% FBS (Gibco) and 1% penicillin/ streptomycin (Gibco) and
453 subcultured every 2-3 days at 1:6 ratio. For all experiments, cells were used between passage
454 59 and 64. HUVE cells were maintained in EBM-2 (Lonza) media with EGM-2 BulletKit (Lonza),
455 2% FBS and 1% penicillin/streptomycin (Gibco) and subcultured every 2-3 days at 1:6 ratio. For
456 all experiments, cells were used between passage 3 and 7. HuH-7 liver epithelial cells were
457 maintained in DMEM with 4.5g/L glucose (HyClone), 10% FBS and 1% penicillin/ streptomycin
458 (Gibco). We also obtained wild-type Huh7 transduced with lentivirus particle pLV[Exp]-Puro-
459 CMV>{Perceval(ns)}:T2A:mCherry/3xNLS (Vector Builder) that were used for live imaging of
460 changes in ATP/ADP ratio within these cells, which directly correlates to cellular metabolic
461 activity.[46] LSEC cells were maintained in EBM-2 (Lonza) media with EGM-2 BulletKit (Lonza),
462 2% FBS and 1% penicillin/streptomycin (Gibco).

463 **Metabolic assays**: Effluents were collected at different timepoints (baseline, 24h, 48h
464 and 1-3 days recovery after washout) throughout the exposure to SNC80 or 1:1000 DMSO
465 vehicle. After treatment, the effluent was collected and analyzed for lactate and glutamate
466 production using the Lactate-Glo™ (Promega, #J5021) and Glutamate-Glo™ (Promega,
467 #J7021) assay kits respectively as per manufacturer protocols.
468 **Cytotoxicity assay**: Cytotoxicity measurements on the Organ Chip effluents were
469 performed using the LDH-Glo™ (Promega, #J2380) as per manufacturer protocols.
470 **ATP/ADP ratio measurements**: Huh7 cells were transfected with a reporter that
471 enables direct measurements of cellular ATP:ADP ratio. The basal excitation spectrum of the
472 reporter protein was similar to that of YFP (peak around 490 nm) but it had an additional peak at
473 CFP wavelength (405 nm). As ATP levels decreased, more ADP can bind to the site,
474 decreasing the YFP/CFP ratio value. BioTek Cytation 5 Cell Imager (Agilent) was used to take
475 RFP, YFP and CFP images of each well every 20min for 180 minutes upon exposure to 100uM
476 SNC80 or 1:100 DMSO vehicle. Post processing of the images was performed using the open
477 source CellProfiler program.[47] We implemented the following pipeline to obtain quantitative
478 ATP/ADP ratio values: (1) Identify nuclei with RFP marker, (2) Define a cell as 4pixels around
479 the edge of the nuclei, (3) Measure cells YFP and CFP intensity and YFP/CFP ratio, (4) Count
480 cells per Image, (5) Track cells YFP and CFP intensity over the time course (0-3h with 20min
481 intervals), (6) Measure YFP/CFP ratio average **over all cells** per image and normalize to cell
482 count (7).
483 For the qualitative images, raw images were processed with ImageJ by using the image
484 calculator to divide yfp/cfp intensity of respective images. “Rainbow RGB” lookup table was
485 used to show the intensity changes. Tones towards the red show more intensity, higher
486 ATP/ADP ratio and higher metabolism.
487 **Organ Chips with Integrated Sensors:** To allow for live oxygen and
488 transepithelial\endothelial resistance (TEER) monitoring, we used our in-house developed and

489 fabricated microfluidic chips with integrated TEER and oxygen sensors. To mimic the in vivo-like
490 cell-cell interface on the models, a dual-channel PDMS microfluidic chip was used where the
491 apical channel is separated from the basal channel with a porous PDMS membrane. A pair of
492 TEER sensing electrodes where integrated on the apical side of the top channel and the basal
493 side of the bottom channel to measure the electrical resistance across the epithelium-
494 endothelium tissue interface. The O_2 sensing nanoparticles (OXNANO, PyroScience) were
495 integrated at four different locations in the chip: two in the apical channel and two in similar
496 locations in the bottom channel. This is to allow a fair representation of the whole chip oxygen
497 tension levels.

498 After fabrication, the chips were sterilized by plasma treatment and desiccated for 30
499 minutes. The polymeric surfaces of the membrane were then chemically functionalized using
500 ER1/ER2 buffers following Emulate^{TM} Inc. protocol and coated with extracellular matrix (ECM)
501 for 1.5-2 hours at 37°C. Gut Chip apical and basal channels were coated with 30 µg/ml
502 Collagen I (Advanced BioMatrix, Cat. no. 5005) and 100 µg/ml Matrigel (BD Biosciences) in cold
503 PBS. Liver Chip apical channel was coated with 30 µg/mL fibronectin (Corning, Cat. no.
504 356008) and 400 µg/mL Collagen I (Advanced BioMatrix, Cat. no. 5005) in cold DPBS, while the
505 basal channel was coated with 100 µg/mL Matrigel (BD Biosciences) and 200 µg/mL type I
506 collagen in cold DPBS. To create Gut Chip, HUVECs (6-8x10^6 cells/ml (P5)) were first seeded
507 on the bottom side of the permeable membrane in the basal channel and incubated for 2-3
508 hours at 37°C before seeding the Caco-2 cells (2-3x10^6 cells/ml (P78)) on the membrane in the
509 apical channel. Liver Chip was similarly created by seeding the LSEC (4-5x10^6 cells/ml (P3-8))
510 the first in the basal channel followed by seeding he Huh7 hepatocytes (2.5-3.5x10^6 cells/ml
511 (P5-15)) on the membrane in the apical channel The chips were then cultured under
512 continuous flow using the commercial culture module instrument (ZOË™ Culture Module,
513 Emulate Inc.,USA). The Gut Chips were maintained under continuous flow of 30µl/hr in the
514 apical and basal channels for 10 days before changing their respective media to differentiation-

515 promoting media (5% FBS in DMED apically and 0.5% FBS endothelial medium basally) for the
516 rest of the culture time. The Liver Chips were also maintained under continuous flow of growth
517 media at 30µl/hr in the apical and basal channels for 5-6 days before reducing the FBS content
518 to 5% in Huh7 media and 0.5% in LSEC media for inducing tissue differentiation.

519 **Human Organ Chip studies:** SNC80 was tested on the Gut Chip at day 16 of culture,
520 when the epithelium showed characteristics of matured, functional tissue and the Liver Chip was
521 tested after 7-10 days of culture. SNC80 [100µM] in the culture media was perfused through the
522 apical and basal channels of the chips at 30µl/hr, while the control chips were perfused with the
523 same culture media containing the compound's vehicle [0.5% DMSO] using the same flow
524 condition. The chips were treated with SNC80 for 48 hours before the drug was removed from
525 the media and the culture was continued for another 4 days. Both Liver and Gut Chips were
526 monitored at d-1, 0h, 3h, 24, 48h timepoints as well as day 1 and 3 after the drug washout for
527 oxygen consumption, TEER measurements, and effluent analysis. Fluorescence microscopy
528 was continuously performed from 0h throughout the treatment period and up to 3 days of
529 recovery. CellProfiler program was used to analyze ATP/ADP ratio as described above.

530 **Oxygen and TEER measurements on-chip:** Oxygen tension level measurements was
531 performed on-chip during the culture using FireSting®-O2 Optical Oxygen and Temperature
532 Meter (FSO2-C4, Pyroscience sensor technology, Germany) connected to Pryo Oxygen Logger
533 (V3.317©, Germany). TEER measurements were performed on-chip using our in-house
534 developed multiplexed TEER Tray and remotely measured from outside the incubator. A four-
535 point impedance measurement was taken on-chip periodically every 24 hours during the SNC80
536 treatment and recovery using the IviumSoft application (V4.97, Informer Technologies, Inc.). To
537 obtain the TEER of only the epithelial-endothelial tissue interface, the measured impedance at
538 100Hz was subtracted from the impedance at 100kHz and reported as the tissue impedance(Ω)
539 throughout the culture and in response to different stimuli as we reported previously.[48]

540 **DNA damage and proliferation assays**: The Click-IT™ EdU cell proliferation kit
541 (Thermofisher, #C10337) was used to assess cell proliferation in the formaldehyde-fixed chips
542 and DNA damage was assessed by staining anti-H2AX antibody (Novus Bio NB100-2280).
543 **Urea Assay**: Urea nitrogen was measured using a colorimetric assay (urea nitrogen
544 test, Stanbio Laboratory), whereby undiluted liver chip effluents were added to a 96 well plate
545 and mixed with the kit's working reagents as per manufacturer protocol.
546 **Albumin Assay**: Liver albumin production was measured using an enzyme-linked
547 immunosorbent assay (Bethyl Laboratories). Liver Chip effluents were diluted 1:100 in buffer
548 before being plated in the kit's 96 well plate, aside from standard wells with dilution series of
549 known albumin concentration solution. We followed manufacturer protocol to perform the
550 sandwich ELISA assay and measure absorbance at 450nm.
551 **Porcine heart ex vivo perfusion studies:** After induction of anesthesia and preparation
552 for clean, non-survival surgery, a median sternotomy was performed followed by longitudinal
553 incision in the pericardium to expose the heart and the great vessels. Following blunt dissection
554 and exposure of the vena cava, aorta and the brachycephalic artery, the superior vena cava,
555 and azygos vein was ligated and divided. The brachycephalic artery was catheterized for
556 infusion of cardioplegia solution. The inferior vena cava was clamped and divided proximal to
557 the clamp. Two or three pulmonary arteries were incised for decompression of the left side of
558 the heart. The aorta was immediately clamped and 10-15 ml/kg of body weight of cold (2-4°C)
559 cardioplegia solution (del Nido without lidocaine, 3 L) was infused at a pressure of 70-80mmHg
560 to stop the heart. Cold 4°C saline and ice were poured over the heart and the accumulated
561 fluids from the thoracic cavity were removed by suction. Following cessation of myocardial
562 function, the heart was removed from the chest by further dissection and division of the
563 pulmonary vessels and aorta distal to the clamp. The heart was cooled in a surgical bowl with
564 cold saline for inspection and preparation for perfusion. All procedures were conducted under

565 the UT Health San Antonio approved Institutional Animal Care and Use Committee (IACUC)
566 protocol 20210080AR.

567 After the heart was removed and placed in a surgical bowl, the aorta and the coronary
568 sinus were cannulated using sterile zip ties. The heart was placed into the VP.S ENCORE®
569 perfusion device filled with 3 L of Krebs-Henseleit buffer supplemented with 20PEG and
570 hemoglobin-based oxygen carrier (HBOC; Hemoglobin Oxygen Therapeutics, LLC, Souderton,
571 PA). The heart was perfused with a pressure of approximately <20 mmHg resulting in a
572 coronary perfusate flow of 50-100 mL/min at a 20-23°C temperature. Hearts were immediately
573 treated with 3 mL of 3% lactic acid containing 135 mg of SNC80 (100 μM final concentration),
574 administered through the arterial line followed by the 3 mL of Krebs-Henseleit flush. Post drug
575 administration, the heart continued to be perfused for additional 6 hours.

576 Two oxygen probes (Pyro FireSting™) collected oxygen partial pressure (mmHg) data of
577 the solution before entering the coronary arteries (arterial) and after exiting the cannulated
578 pulmonary artery (venous), whereas flow was measured using the Sensirion flow meter. Oxygen
579 consumption was captured using the following formula, (([O_2]a- [O_2]v)/100 * Q)/heart weight) *
580 100. [O_2]a and [O_2]v are defined as oxygen content of arterial and venous perfusate
581 respectively. [O_2] was calculated as (1.34 * Hb* SO_2) + (K * pO_2); where 1.34 is mL O_2 / Hb
582 (g), Hb is the concentration of hemoglobin measured in g/dL, SO_2 is the oxygen saturation ratio
583 calculated using the equation developed by Severinghaus,[49] K is the oxygen solubility
584 coefficient adjusted for the perfusate temperature at every data point, pO_2 is the partial pressure
585 of oxygen in mmHg for the perfusate sample, and Q is coronary flow in mL/min.

586 After preservation, hearts were placed on a Langendorff system with a perfusate mixture
587 of 1:1 porcine blood and Krebs-Henseleit buffer. Myocardial oxygen consumption
588 (MVO_2 mLO_2 /min / 100g) was calculated during an initial 30 min of rewarming stage (before
589 defibrillation) and after defibrillation using two oxygen probes (Pyro FireSting™, placed in

590 arterial and venous effluent). Oxygen consumption was [53]calculated using the same approach
591 described for the VP.S ENCORE® perfusion stage. The left ventricular function was expressed
592 as dP/dT (mmHg/sec) measured by placing a pressure catheter (Millar, 5F) in the left ventricle.
593 Data was analyzed using PowerLab (LabChart 8.1.16) blood pressure analyzer. Data was
594 selected from the left ventricular pressure waveform as the average of 30 beats after
595 stabilization (approx. 30 minutes after defibrillation). Contractility after ionotropic support was
596 measured less than 5 minutes after administration of epinephrine (0.5mg injected arterial). End
597 diastolic pressure of the left ventricle was maintained 5.14 +/- 1.89 mmHg through administering
598 perfusate directly into the left ventricle through the pulmonary veins and venting to
599 atmosphere.

600 ECG data were obtained through the placement of leads on the apex (positive), right
601 atrial appendage (negative), and aortic root (ground). Data was collected through the PowerLab
602 system and 30-second time intervals were selected for all groups before the flush, before
603 defibrillation, at native contraction, and after epinephrine drug administration. The ECG
604 amplitude (mV) was analyzed using LabChart Pro (v8.1.19) peak analysis detection at
605 approximate time points 10min (before flush) and 30min (before defibrillation) to detect the
606 average amplitude of electrical activity without full contraction. LabChart Pro (v8.1.19) ECG
607 Analysis detection was used at time points 35min (Epinephrine) and 60min (Native) to detect
608 the average amplitude of the QRS complex with contraction. The native QRS Interval (s) and ST
609 Height (mV) was averaged over a 30-second time interval using LabChart Pro (v8.1.19) ECG
610 Analysis.

611 Total RNA from cardiac tissue biopsies (2.5 mm) were extracted following the RNeasy
612 Mini kit (Qiagen) according to the manufacturer's instructions. The concentration of total RNA
613 was evaluated and measured at 260/280nm by spectrophotometer (NanoVue Plus, GE
614 Healthcare). Synthesis of cDNA was performed from 0.5 µg of total RNA, which was reverse
615 transcribed using (iScript cDNA Synthesis Kit, Bio-Rad) according to the manufacturer's

616 instructions. Gene-specific pre-designed oligonucleotide primers were purchase from Sigma.
617 qRT-PCR was done using SsoAdvanced Universal SYBR Green Supermix and SFX96 Touch
618 real time PCR detection system (Bio-Rad, T100 Thermal Cycler). The cycling parameters were
619 as follows: initial denaturation 95°C, 2 min; denaturation 95°C, 5 s; annealing/extension 60°C,
620 30 s; number of cycles 40; melt curve 65°-95°C (0.5°C increments). The comparative CT (2-
621 ΔΔCT) method was used for all quantification. Values were normalized to the Gapdh
622 housekeeping gene.

623 **Porcine limb ex vivo perfusion studies:** Hindlimbs (N=8) were procured via protocol
624 tissue sharing at the Joint Base San Antonio Clinical Investigation and Research Support
625 (CIRS) building, following IV Pentobarbital euthanasia, 100 mg/kg from a host protocol. Host
626 protocol animals were treated with the same surgical manipulations and no chemicals or drugs
627 were introduced experimentally prior to euthanasia. Following euthanasia, a curvilinear incision
628 was made around the hindlimb circumferentially. Subsequently, the neurovascular pedicle in the
629 medial hindlimb was identified and carefully dissected out to preserve the vascular bundle. The
630 pedicle was then divided at the origin of the artery and vein to preserve maximal length of the
631 vessels. Hindlimb bone was separated using a Gigli Saw. Hindlimbs were cannulated through
632 the femoral artery and underwent immediate arterial flush with up to 200-400 mL heparinized-
633 saline solution (10,000 units of heparin per 1L of saline), until venous outflow was clear.
634 Additionally, the femoral vein was cannulated for measurement and collection of venous outflow
635 samples.

636 Limbs were divided into two groups, control (N=3) and experimental SNC80 (N=5). All
637 hindlimbs were connected to the ENCORE® head for perfusion via the cannulated femoral
638 artery. The femoral vein was cannulated for obtaining venous samples. Hindlimbs were
639 perfused with oxygenated Krebs-Henseleit (KH) at ambient temperature. Arterial and venous
640 pO2 were assessed hourly using a commercial blood gas analyzer (ALB1000 by Radiometer,
641 Brea, California USA). Oxygen consumption was calculated from A-V differences obtained from

642 arterial and venous blood gas readings. After 3 hours of perfusion (baseline), torpor inducing
643 compound SNC80 (44.96 µg/ml) was administered via the femoral artery to the experimental
644 group (SNC80) (N=5) and an equal volume of the sham vehicle to the control limbs (N=3)
645 followed by and additional 3 hours of perfusion (drug). The hind limbs were then removed from
646 the perfusor and flushed with fresh KH perfusate and replaced into the perfusor containing fresh
647 KH solution (flush). The perfusion then resumed for an additional 6 hours. The hindlimbs were
648 weighed pre and post perfusion. Biopsy tissue samples were taken at baseline (pre-ENCORE®),
649 and before and after the administration of the SNC80 compound for RNA-Seq analysis and
650 histological evaluation.

651 Biopsies for histopathology were obtained superficially from the rectus femoris muscle
652 bundle immediately after amputation and then 24 hours after the perfusion period. Biopsies
653 were stored in 10% formalin for 24 hours and then stored for 3 days in 70% ethanol and
654 embedded in paraffin. The samples were sectioned into 5µm slides and stained with
655 hematoxylin and eosin (H&E) to evaluate tissue morphology, intracellular distance, muscle
656 bundle area, and Periodic Acid-Schiff to evaluate glycogen content. Histological analysis was
657 performed by visualizing slides under a light microscope (AM Scope T670Q, Irvine, California)
658 and capturing images using a high-definition camera (AM Scope Model# MU2003B1, Irvine,
659 California). From each slide, 10 digital images from randomly selected fields were obtained at
660 10x magnification. The images were de-identified and evaluated for intracellular distance,
661 muscle bundle area and glycogen content by two independent reviewers using Image J
662 software (v.1.51.).

663 **Statistical analysis.** All graphing and statistical analyses were performed with Prism 9
664 (GraphPad Software Inc., La Jolla, CA, USA) with a (two-sided) significance level of 0.05.
665 Statistical tests and corrections for multiple comparisons are described in each figure panel.
666

667 **Data availability statement**

The proteomics data reported in this paper have been deposited in the Mass Spec Interactive Virtual Environment, MassIVE, (accession no. MSV000091410). All other data are available within the paper and its Supplementary Information files.

Software availability statement

A custom Python script was used to automatically count heart beat in *Xenopus* tadpoles. This code can be accessed on GitHub: https://github.com/k-shcherb/heart_seg.

Acknowledgements

The authors gratefully acknowledge funding from the Army Research Office/DARPA under Cooperative Agreement Number W911NF-19-2-0027. The views and conclusions contained in this document are those of the authors and should not be interpreted as representing the official policies, either expressed or implied, of the Army Research Office/DARPA or the U.S. Government. The U.S. Government is authorized to reproduce and distribute reprints for Government purposes notwithstanding any copyright notation herein. M.P.O. acknowledges financial support from the Margarita Salas postdoctoral grant (UNI/551/2021). We thank E. Switzer for Xenopus embryo fertilization; R. Colon, S. Sundar, and E. Lederer for Xenopus embryo husbandry and transport organization; members of the Levin Lab, Tufts University for useful discussions; and R. Gould for help with database extraction. Image analysis workflows were created in consultation with D. Stirling and B. Cimini of the Broad Institute Imaging Platform.

Author Contributions

R.N., M.Su., and D.E.I. conceived of and directed the work. M.M.S., H.F., E.G., A.K., S.K., M.P.O., K.She., and T.L. performed *Xenopus* studies with guidance from R.N. and M.Lev. R.M. developed and maintained engineered components for *Xenopus* assays. H.F., M.M.S., A.K.,

M.P.O., and T.T. analyzed *Xenopus* data. T.L. and M.Lew. performed MALDI-TOF experiments and analyzed the data. B.C., K.P., and Z.I. performed in vitro and Organ Chip studies and analyzed data with guidance from A.M.S. S.M. and K.Shc. designed, assembled, and maintained custom microscopy equipment for Organ Chip imaging. K.Shc. analyzed imaging data from tadpole and in vitro experiments. S.L. oversaw compound management and material transfers. J.M. designed novel chemical entities. Porcine heart experiments were conceived and directed by R.V. and L.B and experiments were designed and interpreted by R.V., L.B., and K.A. Porcine heart data analysis was performed by R.V., L.B., K.A, E.C., R.L., I.C., Z.M., and D.D.C. Porcine heart data was acquired by K.A, E.C., R.L., I.C., and Z.M. Porcine limb studies were conceived and directed by R.V., L.B., E.W., and T.P. Porcine limb surgeries were performed by J.Y., O.P., and J.S. Porcine limb sampling and data analysis were performed by R.V., L.B., J.P., D.W., Z.H., C.H. and J.C.H. M.M.S., B.C., K.P., Z.I., T.L., K.A., R.N. and D.E.I. drafted the manuscript and all authors reviewed and provided critical input for the manuscript.

Competing Interests

D.E.I. is a founder, board member and Scientific Advisory Board chair of, and holds equity in, Emulate Inc. M.Le., R.N., M.M.S., E.G., T.T., and D.E.I are inventors on a relevant patent application held by Harvard University (PCT/US2021/012626). R.N., E.G., M.Le., and D.E.I. hold equity in Unravel Biosciences, Inc.; R.N. and D.E.I. are members of its board of directors; M.Le. and D.E.I. are members of its scientific advisory board; and R.N. and E.G. are current employees of the company. R.V., L.B., K.A, E.C., R.L., I.C., and Z.M are employees of Vascular Perfusion Solutions. D.E.I. is a member of its scientific advisory board. The remaining authors declare no competing interests.

References

1. Vela, R. J., Jessen, M. E. & Peltz, M. Ice, ice, maybe? Is it time to ditch the igloo cooler? Benefits of machine perfusion preservation of donor hearts. *Artificial Organs* vol. 44 220–227 Preprint at https://doi.org/10.1111/aor.13599 (2020).
2. Petrenko, A. *et al.* Organ Preservation into the 2020s: The Era of Dynamic Intervention. *Transfusion Medicine and Hemotherapy* vol. 46 151–172 Preprint at https://doi.org/10.1159/000499610 (2019).
3. Guibert, E. E. *et al.* Organ preservation: Current concepts and new strategies for the next decade. *Transfusion Medicine and Hemotherapy* vol. 38 125–142 Preprint at https://doi.org/10.1159/000327033 (2011).
4. Andrijevic, D. *et al.* Cellular recovery after prolonged warm ischaemia of the whole body. *Nature* (2022) doi:10.1038/s41586-022-05016-1.
5. Tessier, S. N. *et al.* Partial freezing of rat livers extends preservation time by 5-fold. *Nat Commun* **13**, 4008 (2022).
6. Hrvatin, S. *et al.* Neurons that regulate mouse torpor. *Nature* **583**, 115–121 (2020).
7. Takahashi, T. M. *et al.* A discrete neuronal circuit induces a hibernation-like state in rodents. *Nature* **583**, 109–114 (2020).
8. Dou, M., Lu, C. & Rao, W. Bioinspired materials and technology for advanced cryopreservation. *Trends in Biotechnology* vol. 40 93–106 Preprint at https://doi.org/10.1016/j.tibtech.2021.06.004 (2022).
9. Blackstone, E., Morrison, M. & Roth, M. B. H2S induces a suspended animation-like state in mice. *Science (1979)* **308**, 518 (2005).
10. Beal, E. W. *et al.* [D-Ala 2 , D-Leu 5] Enkephalin Improves Liver Preservation During Normothermic Ex Vivo Perfusion. *Journal of Surgical Research* **241**, 323–335 (2019).
11. Ratigan, E. D. & McKay, D. B. Exploring principles of hibernation for organ preservation. *Transplantation Reviews* vol. 30 13–19 Preprint at https://doi.org/10.1016/j.trre.2015.08.002 (2016).
12. Rawls, S. M., Hewson, J. M., Inan, S. & Cowan, A. Brain delta2 opioid receptors mediate SNC-80-evoked hypothermia in rats. *Brain Res* **1049**, 61–69 (2005).
13. Horiuchi, T. *et al.* The Effects of the δ-Opioid Agonist SNC80 on Hind-Limb Motor Function and Neuronal Injury After Spinal Cord Ischemia in Rats. *Anesth Analg* **99**, 235–240 (2004).
14. Sperry, M. M. *et al.* Enhancers of host immune tolerance to bacterial infection discovered using linked computational and experimental approaches. *Advanced Science* (2022).
15. Novak, R. *et al.* Target-agnostic discovery of Rett Syndrome therapeutics by coupling computational network analysis and CRISPR-enabled in vivo disease modeling. *bioRxiv* (2022) doi:10.1101/2022.03.20.485056.
16. Schmitt, S. M., Gull, M. & Brändli, A. W. Engineering Xenopus embryos for phenotypic drug discovery screening. *Adv Drug Deliv Rev* **69–70**, 225–246 (2014).
17. Sullivan, K. G. & Levin, M. Inverse drug screening of bioelectric signaling and neurotransmitter roles: Illustrated using a Xenopus tail regeneration assay. *Cold Spring Harb Protoc* **2018**, 154–163 (2018).
18. Giroud, S. *et al.* Lipidomics reveals seasonal shifts in a large-bodied hibernator, the brown bear. *Front Physiol* **10**, (2019).
19. Kolomiytseva, I. K. Lipids in mammalian hibernation and artificial hypobiosis. *Biochemistry (Moscow)* vol. 76 1291–1299 Preprint at https://doi.org/10.1134/S0006297911120029 (2011).
20. Soeters, M. R. *et al.* Muscle acylcarnitines during short-term fasting in lean healthy men. *Clin Sci* **116**, 585–592 (2009).

21. Welinder, K. G. *et al.* Biochemical foundations of health and energy conservation in hibernating free-ranging subadult brown bear ursus arctos. *Journal of Biological Chemistry* **291**, 22509–22523 (2016).
22. Otis, J. P., Sahoo, D., Drover, V. A., Yen, C. L. E. & Carey, H. v. Cholesterol and lipoprotein dynamics in a hibernating mammal. *PLoS One* **6**, (2011).
23. Jones, L. L., McDonald, D. A. & Borum, P. R. Acylcarnitines: Role in brain. *Progress in Lipid Research* vol. 49 61–75 Preprint at https://doi.org/10.1016/j.plipres.2009.08.004 (2010).
24. Petrov, A., Kasimov, M. & Zefirov, A. Brain Cholesterol Metabolism and Its Defects: Linkage to Neurodegenerative Diseases and Synaptic Dysfunctio. *Acta Naturae* **8**, 58–73 (2016).
25. Veraza, R. *et al.* (872) Preclinical Evaluation of the VP.S ENCORE^{TM} Cardiac Preservation Device. *The Journal of Heart and Lung Transplantation* **42**, S379 (2023).
26. Andrijauskaite, K. *et al.* (399) Novel Portable Hypothermic Perfusion Preservation Device Enhances Cardiac Output of Donated Human Hearts. *The Journal of Heart and Lung Transplantation* **42**, S188 (2023).
27. Kaltenborn, A. *et al.* Ex vivo limb perfusion for traumatic amputation in military medicine. *Mil Med Res* **7**, (2020).
28. Ralphe, J., Segar, J., Schutte, B. & Scholz, T. Localization and function of the brain excitatory amino acid transporter type 1Bin cardiac mitochondria. *J Mol Cell Cardiol* **37**, 33–41 (2004).
29. Maiolino, M. *et al.* Essential role of the Na+-Ca2+ exchanger (NCX) in glutamate-enhanced cell survival in cardiac cells exposed to hypoxia/reoxygenation. *Sci Rep* **7**, 13073 (2017).
30. Magi, S. *et al.* Glutamate-induced ATP synthesis: Relationship between plasma membrane Na+/Ca2+ exchanger and excitatory amino acid transporters in brain and heart cell models. *Mol Pharmacol* **84**, 603–614 (2013).
31. Magi, S., Piccirillo, S. & Amoroso, S. The dual face of glutamate: from a neurotoxin to a potential survival factor—metabolic implications in health and disease. *Cellular and Molecular Life Sciences* vol. 76 1473–1488 Preprint at https://doi.org/10.1007/s00018-018-3002-x (2019).
32. Magi, S., Piccirillo, S. & Amoroso, S. The dual face of glutamate: from a neurotoxin to a potential survival factor—metabolic implications in health and disease. *Cell. Mol. Life Sci.* **76**, 1473–1488 (2019).
33. Chiba-Falek, O., Gottschalk, W. K. & Lutz, M. W. *The effects of the TOMM40 poly-T alleles on Alzheimer's disease phenotypes*. (2018).
34. Ingber, D. E. Human organs-on-chips for disease modelling, drug development and personalized medicine. *Nature Reviews Genetics* vol. 23 467–491 Preprint at https://doi.org/10.1038/s41576-022-00466-9 (2022).
35. Si, L. *et al.* A human-airway-on-a-chip for the rapid identification of candidate antiviral therapeutics and prophylactics. *Nat Biomed Eng* (2021) doi:10.1038/s41551-021-00718-9.
36. Kim, H. J., Li, H., Collins, J. J. & Ingber, D. E. Contributions of microbiome and mechanical deformation to intestinal bacterial overgrowth and inflammation in a human gut-on-a-chip. *Proc Natl Acad Sci U S A* **113**, E7–E15 (2016).
37. Choi, Y. Y., Kim, J., Lee, S. H. & Kim, D. S. Lab on a chip-based hepatic sinusoidal system simulator for optimal primary hepatocyte culture. *Biomed Microdevices* **18**, (2016).
38. Ewart, L. *et al.* Qualifying a human Liver-Chip for predictive toxicology: Performance assessment and economic implications. *bioRxiv* 2021.12.14.472674 (2021) doi:10.1101/2021.12.14.472674.

39. Kon, N. *et al. Na + /Ca 2+ exchanger mediates cold Ca 2+ signaling conserved for temperature-compensated circadian rhythms*. *Sci. Adv* vol. 7 http://advances.sciencemag.org/ (2021).
40. Shah Amran, M., Homma, N. & Hashimoto, K. *Pharmacology of KB-R7943: A Na +-Ca 2+ exchange inhibitor-sion arrhythmia-KB-R7943-Na +-Ca 2+ exchange (NCX1-3)-NCX inhibitors-Ni 2+-SEA0400-SN-6*. (2003).
41. Schafer, C. *et al. Role of the reverse mode of the Na / Ca exchanger in reoxygenation-induced cardiomyocyte injury*. *Cardiovascular Research* vol. 51 www.elsevier.com/locate/cardiores (2001).
42. Headrick, J. P., See Hoe, L. E., Du Toit, E. F. & Peart, J. N. Opioid receptors and cardioprotection-'opioidergic conditioning' of the heart Correspondence LINKED ARTICLES. *Br J Pharmacol* **172**, 2026–2050 (2015).
43. Pugsley, M. K. The diverse molecular mechanisms responsible for the actions of opioids on the cardiovascular system. *Pharmacol Ther* **93**, 51–75 (2002).
44. Bankhead, P. *et al.* QuPath: Open source software for digital pathology image analysis. *Sci Rep* **7**, (2017).
45. Goto-Inoue, N., Kashiwagi, A., Kashiwagi, K. & Mori, T. Metabolomic approach for identifying and visualizing molecular tissue markers in tadpoles of Xenopus tropicalis by mass spectrometry imaging. *Biol Open* **5**, 1252–1259 (2016).
46. Berg, J., Hung, Y. P. & Yellen, G. A genetically encoded fluorescent reporter of ATP:ADP ratio. *Nat. Methods* **6**, 161–166 (2009).
47. Stirling, D. R. *et al.* CellProfiler 4: improvements in speed, utility and usability. *BMC Bioinformatics* **22**, (2021).
48. Henry, O. Y. F. *et al.* Organs-on-chips with integrated electrodes for trans-epithelial electrical resistance (TEER) measurements of human epithelial barrier function. *Lab Chip* **17**, 2264–2271 (2017).
49. Severinghaus, J. W. *Simple, accurate equations for human blood 02 dissociation computations*. (1979).

850 ## Figure Legends

851 **Figure 1. SNC80 treatment in *Xenopus* tadpoles. a.** Swimming activity of *Xenopus*
852 during 100μM SNC80 or vehicle treatment. Data represent the mean±SD of n=3 replicates, with
853 10 tadpoles per replicate. **b.** Oxygen consumption rate for *Xenopus* treated with SNC80 or
854 vehicle controls. N=5 medium only, n=7 vehicle and n=9 SNC80, with each data point
855 representing the cumulative oxygen consumption for 5 tadpoles. **c.** Heart rate in SNC80 and
856 vehicle-treated *Xenopus* (n=10 tadpoles/group). Statistical comparisons were performed using a
857 Brown-Forsythe and Welch ANOVA test with a Dunnett correction for multiple comparisons (**b**)
858 and a 2-way ANOVA (treatment x timepoint) with Tukey correction for multiple comparisons (**c**).
859 Bar plots show the mean±SD of each group.

860 **Figure 2. SNC80 uptake and activity at the delta opioid receptor. a.** Distribution of
861 SNC80 in *Xenopus* tadpoles after 1 and 2 hours of compound exposure. **b.** Uptake of SNC80 in
862 the tadpole skeletal muscle, GI tract, and gills at 1 and 2 hours of exposure. **c.** Levels of
863 acylcarnitine and cholesterol ester in the skeletal muscle and brain after 1 hour of SNC80
864 treatment. *In vivo* distributions of SNC80 and lipid levels measured from N=5 tadpoles per
865 condition; N=3 sections/slide. **d.** Oxygen consumption in *Xenopus* tadpoles treated with SNC80,
866 the delta opioid antagonist naltrindole, or a combination of SNC80 and naltrindole. N=3
867 replicates/group with each data point representing the cumulative oxygen consumption from 5
868 tadpoles. Statistical comparisons were performed using a two-way ANOVA (time x tissue
869 region) with Sidak's correction for multiple comparisons (**b**), multiple unpaired t-tests for each
870 tissue region with FDR correction (**c**), and a Welch ANOVA test with Dunnett correction for
871 multiple comparisons between vehicle and each treatment group (**d**). Bar plots show the
872 mean±SD of each group.

873 **Figure 3. Design and *in vivo* screening of novel analog WB3. a.** Molecular structures
874 for SNC80 and novel compound WB3. **b.** Percent specific binding of the delta opioid receptor

875 radioligand [3H]-DADLE in the presence of SNC80 and WB3. c. Swimming activity of *Xenopus*
876 during 100μM WB3, SNC80, or vehicle treatment. Data represent the mean±SD of n=2
877 replicates, with 10 tadpoles per replicate. **d.** Heart rate in WB3 and vehicle-treated *Xenopus*
878 (n=10 tadpoles/group). Statistical comparisons were performed using a two-way ANOVA (group
879 x timepoint) with Sidak correction for multiple comparisons (**d**). Bar plots show the mean±SD of
880 each group.

881 **Figure 4. Preservation of porcine cardiac grafts with SNC80 over 6 hours. a.**
882 Oxygen consumption for vehicle and SNC80-treated cardiac grafts perfused in the VP.S
883 ENCORE® device (n=3 hearts/group). **b.** Oxygen consumption during cardiac reperfusion on the
884 Langendorff system before defibrillation (n=3 vehicle and n=3 SNC80 hearts). **c.** Oxygen
885 consumption measured on the Langendorff system after defibrillation (n=3 vehicle and n=3
886 SNC80 hearts). **d.** Left ventricle (LV) contractility and relaxation before and after defibrillation
887 and tissue exposure to epinephrine (n=3 vehicle and n=2 SNC-treated hearts). **e.** Gene
888 expression analysis of heart biopsy samples for vehicle and SNC80-treated cardiac grafts (n=2
889 hearts/group; 3 technical replicates each). **f.** Light microscopic views of H&E-stained histological
890 sections of heart biopsies (20x magnification) after 6 hours of perfusion. Statistical comparisons
891 were performed using multiple unpaired t-tests between SNC80 and vehicle-treated cardiac
892 grafts (**a,b,c**), two-way ANOVA with Sidak correction for multiple comparisons between SNC80
893 and vehicle-treated cardiac grafts (**d**), and unpaired t-tests between SNC80 and vehicle for each
894 gene of interest (**e**). Data represent the mean±SD.

895

896 ## Tables

897 **Table 1. SNC80 protein binding targets identified by thermal proteome profiling.**

898

899 ## Supplemental Figure Legends

900 **Figure S1. Metabolic measurements in SNC80-treated *Xenopus* embryos.** Oxygen
901 consumption rate in *Xenopus* embryos treated with SNC80 (n=3-4 replicates/group). Statistical
902 comparisons were performed using a Brown-Forsythe and Welch ANOVA test with Dunnett
903 correction for multiple comparisons between untreated and each treatment group. Data
904 represent the mean±SD.

905 **Figure S2. Preservation of whole porcine limbs with SNC80. a.** The relative
906 metabolic rate at baseline is not statistically significantly different between control (n=3) and
907 SNC80 (n=5) injected limbs. Metabolic rate is reduced during the treatment and washout
908 phases for SNC80 relative to controls. **b.** Mean muscle bundle area between T0 before SNC80
909 administration and at T3 after SNC80 administration and histographs of limb biopsy (20x
910 magnification) at T0 before SNC80 administration and T3 after SNC80 administration. Muscle
911 bundle area is not affected by the administration of SNC80. **c.** Optical density between T0
912 before SNC80 administration and at T3 after SNC80 administration and histographs of limb
913 biopsy (20x magnification) at T0 before SNC80 administration and T3 after SNC80
914 administration. Optical density is not affected by the administration of SNC80. **d.** Mean
915 intracellular distance during T0 before SNC80 administration versus T3 after SNC80
916 administration and histographs of limb biopsy (10x magnification) at T0 before SNC80
917 administration and T3 after SNC80 administration. Red arrows indicate intracellular distance
918 measured. Intracellular distance increases after the administration of SNC80. Statistical
919 comparisons were performed using a mixed-effects analysis with a Sidak's test for multiple
920 comparisons (a) and Welch's t-test (b-d). Data represent the mean±SD.

921 **Figure S3. Characterization of human Gut and Liver Chips with integrated sensing**
922 **technology. a.** Illustration of the sensor-integrated OOC unit connected to reservoir pod for
923 automatic operation of fluid flow using pneumatic pressure (left). Inset shows a schematic of the
924 top and bottom views of the sensor-chip-PCB compartment showing locations of TEER

925 electrodes and O_2 sensors in the apical and basal channels. Four O_2 sensing spots were added
926 to the channels - two in the top and two in the bottom channels for across the chip
927 measurement. Electrode connectors are necessary for remote TEER sensing. **b.** Phase contrast
928 images of Caco-2 cells seeded on sensor-chip at day 1, and 10 of culture (top) and Huh7 cells
929 seeded on sensor-chip at day 1 and 10 (middle). Fluorescent images of liver chip at day 1 and
930 10 of the transduced nuclear marker (bottom) **c.** Percentage of O2 level (black) and TEER
931 impedance values (gray) on sensor Liver Chip during 10 days of culture. **d**. Average albumin
932 production of Liver Chips at day of experiment start (day 7-10 of culture). **e**. Average urea
933 production of Liver Chips at day of experiment start (day 7-10 of culture). **f.** Representative
934 immunofluorescence images of the sensor Gut Chip (left) and Liver Chip (right) epithelium
935 stained with DNA damage marker (H2AX) and nuclei (DAPI) for vehicle control and SNC80
936 treated tissues after 7 days recovery. **g.** Quantitative analysis of proliferation and DNA damage
937 stains on Gut and Liver Chips after 48h of treatment and 7-day recovery to 100μM SNC80 (2-3
938 biological replicates/group/marker). Statistical comparisons were performed using multiple
939 unpaired t-tests for each marker with FDR correction. Data represent the mean±SD.

940 **Figure S4. SNC80 treatment in human Organ Chips. a.** Monitoring changes in O_2
941 levels in human Gut (dotted lines; n=6 Chips/group) or Liver (straight lines; n=15-16
942 Chips/group) Chips throughout the treatment with 100 μM SNC80 (0-48h) and recovery (48-
943 120h) versus vehicle control Chip. **b.** Graph showing the quantitative drop in ATP/ADP ratio of
944 Liver Chip treated for 48h with 100μM SNC80 or Vehicle control as well as 2 days recovery after
945 drug washout (n=5 control and n=3 SNC80 Chips). Statistical comparisons were performed
946 using multiple unpaired t-tests for each timestamp with multiple comparison between control
947 and treated cells. Data represent the mean±SD.

948 **Figure S5. Metabolic measurements of Gut and Liver Chip systems treated with**
949 **SNC80. a.** Monitoring the percentage change in barrier function of Gut (n=6 Chips/group) or **b**.

950 Liver Chip (n=9 Chips/group) with time during treatment with 100μM SNC80 (0-48h) and
951 recovery (48-120h) versus vehicle control Chip. **c**. Cytotoxicity measured for the Gut and **d.**
952 Liver Chips during treatment and recovery. **e**. Graph depicting the amount of lactate measured
953 in effluents of Gut and **f**. Liver Chips post recovery (day 7 for Gut and day 5 for Liver) for
954 SNC80-treated (red) or vehicle control (black) Chips. **g**. Graph showing the glutamate measured
955 in effluents of Gut or **h**. Liver Chips during SNC80 (red) or vehicle (black) treatment and post
956 recovery (day 7). For each measurement, statistical comparisons were performed using multiple
957 unpaired t-tests at each timepoint and FDR correction for multiple comparisons. Data represent
958 the mean±SD.

959 **Table S1. Clinical interpretation of ECG in SNC80 and vehicle treated hearts.**

960

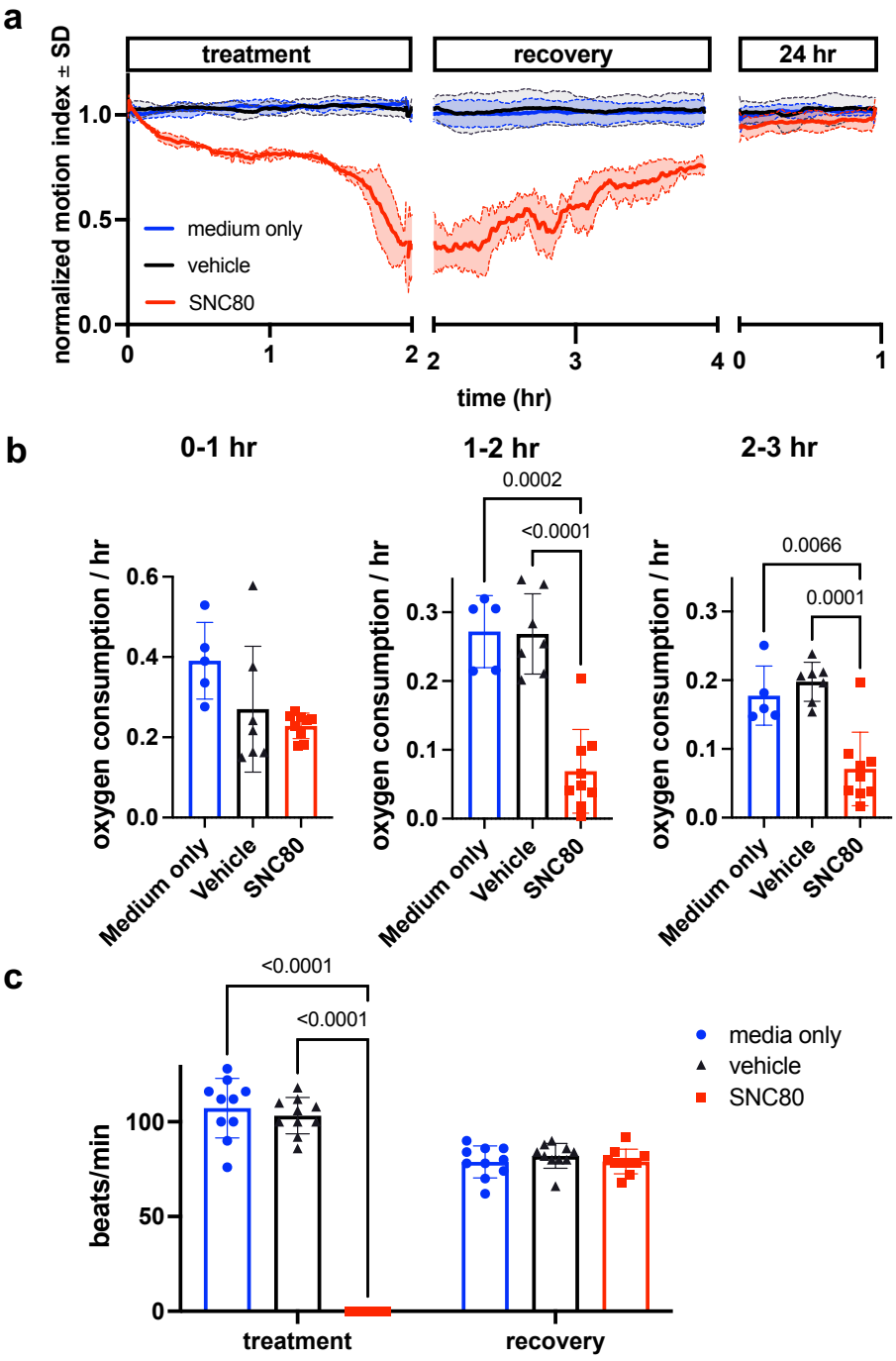

Figure 1

961

962

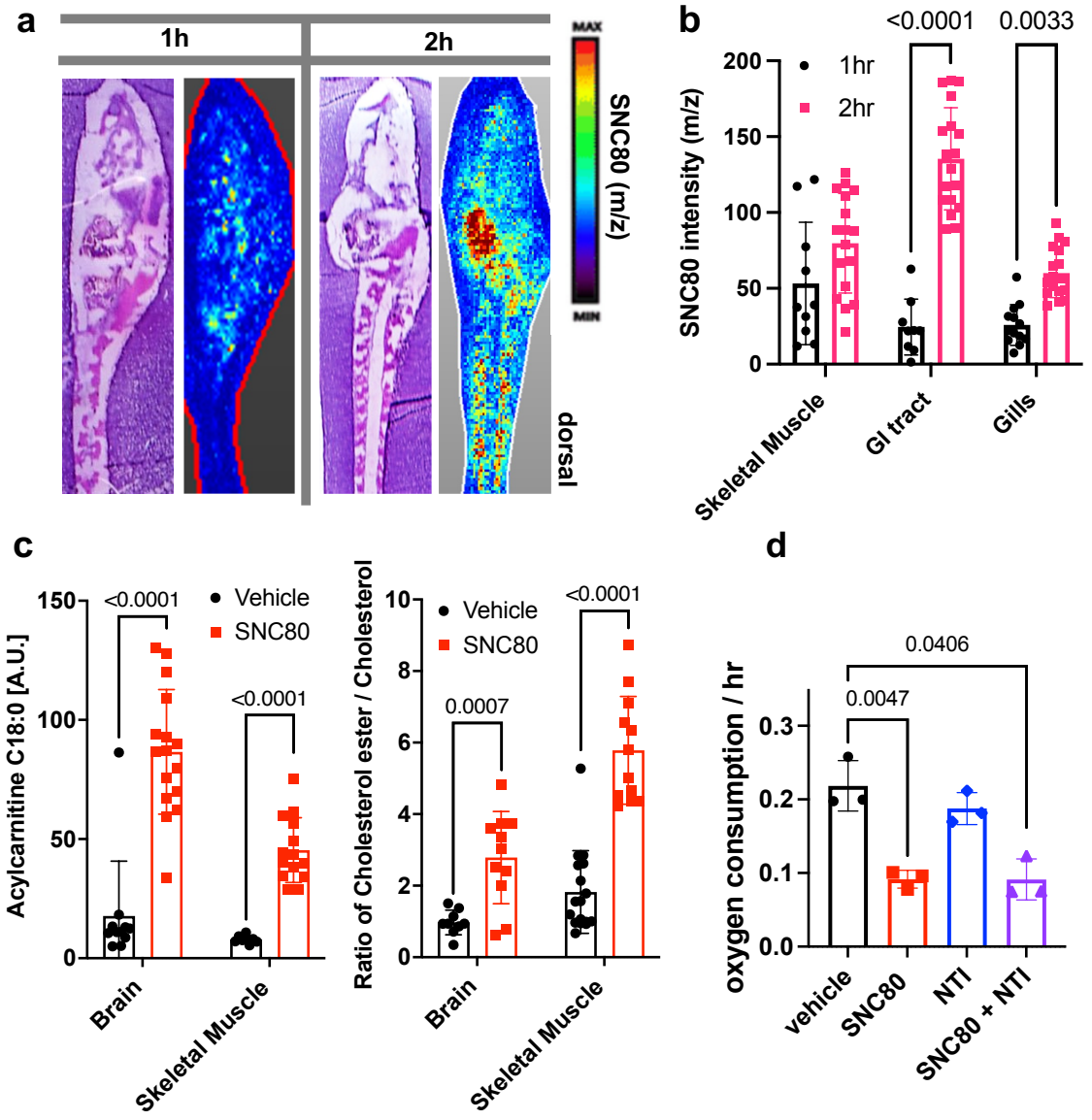

Figure 2

963

964

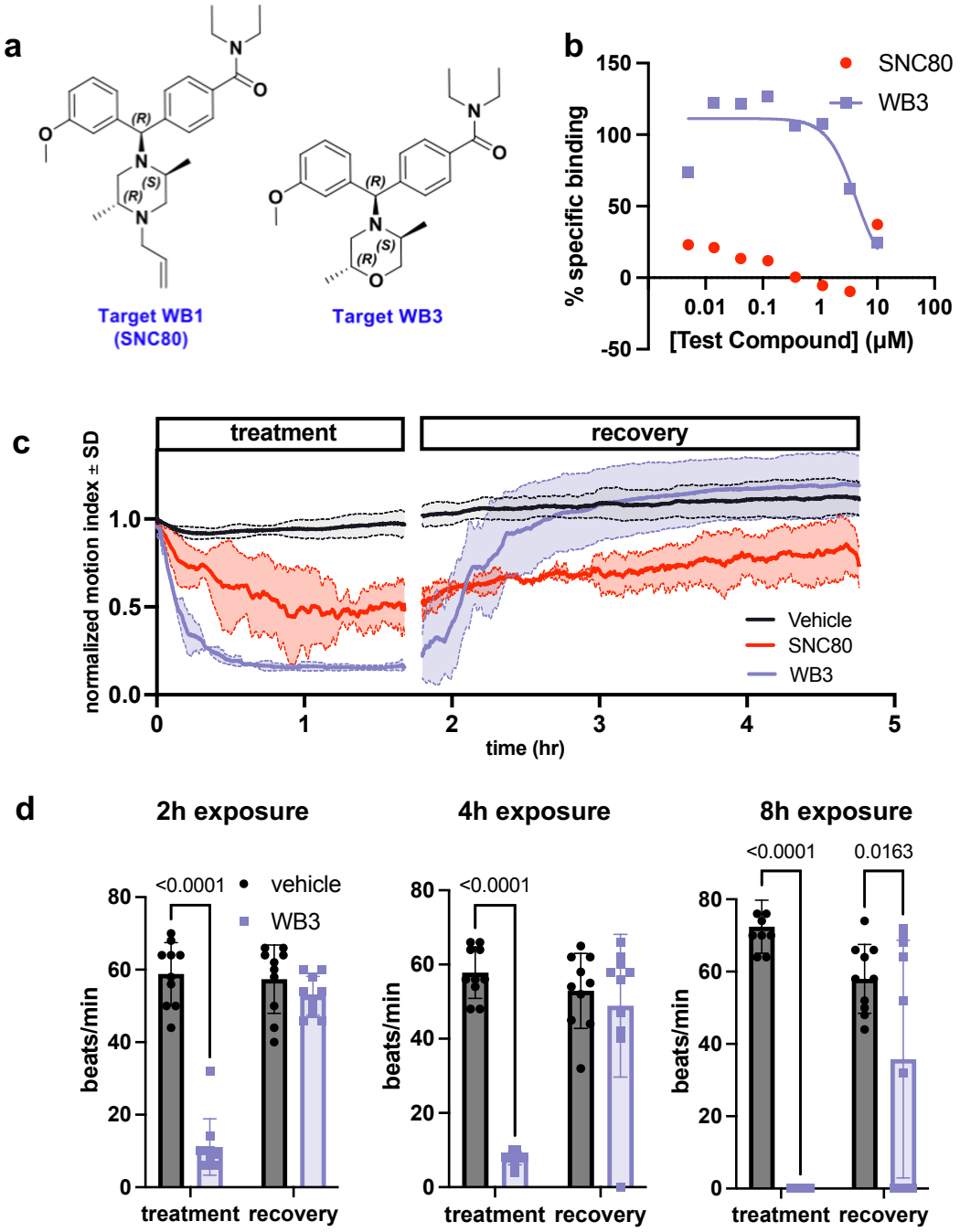

Figure 3

965

966

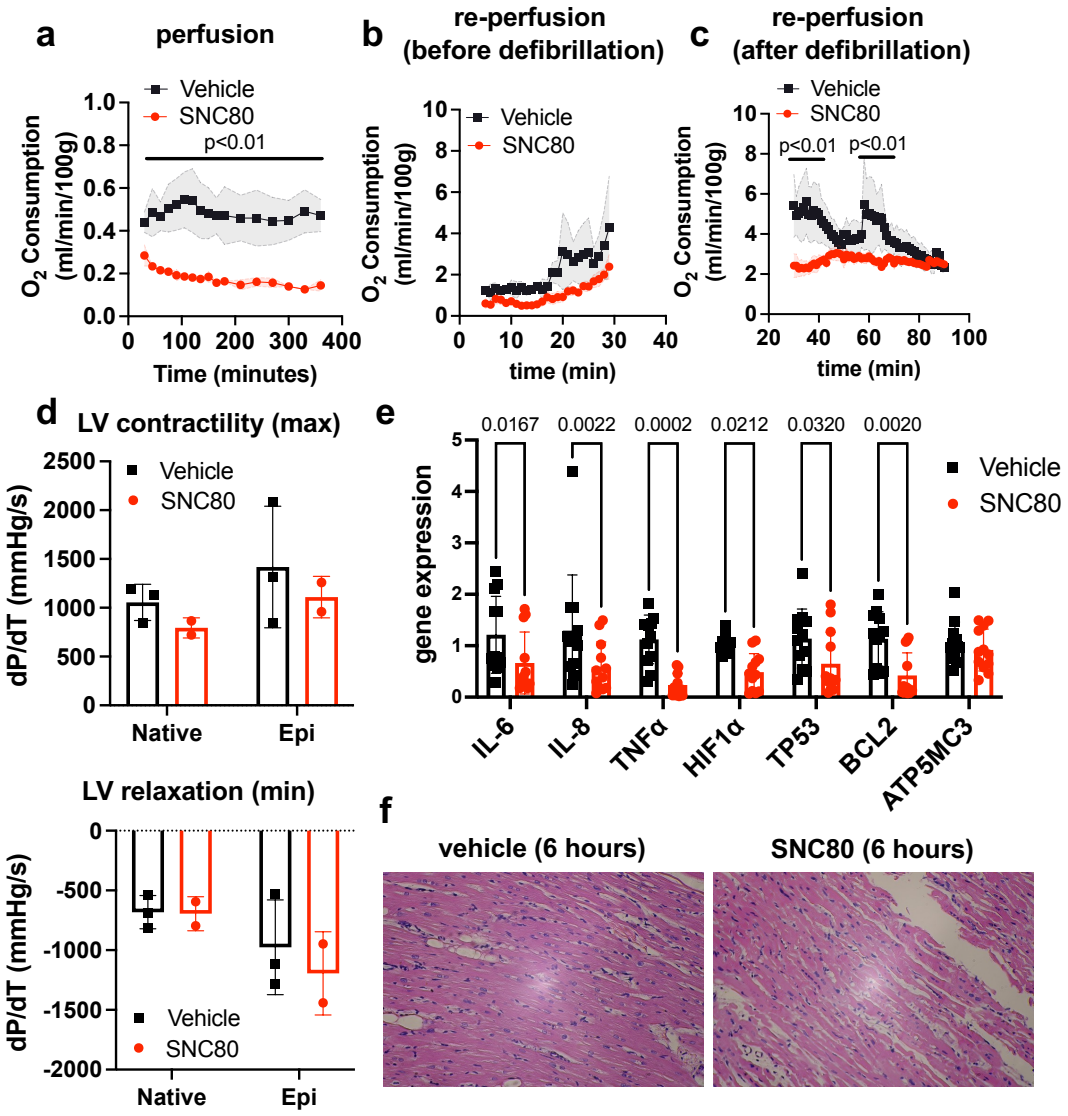

Figure 4

967

968

969

direct interaction	function	indirect interaction	function
CCBL1	• pyridoxal phosphate binding • cysteine-S-conjugate beta-lyase activity • L-glutamine aminotransferase activity • cellular modified amino acid metabolic process	ABCB1	• ABC-type bile acid transporter activity • regulation of fatty acid beta-oxidation • efflux transmembrane transporter activity
EAAT1	• L-glutamate transmembrane transporter activity	ACOX3	• fatty acid beta-oxidation using acyl-CoA oxidase • fatty acid binding
FUCA2	• alpha-L-fucosidase activity • glycoside catabolic process	CAMSAP2	• cytoplasmic microtubule organization • calmodulin binding
HM13	• peptidase activity • aspartic endopeptidase activity	COX6C	• mitochondrial electron transport, cytochrome c to oxygen • generation of precursor metabolites and energy
PTX3	• negative regulation of glycoprotein metabolic process • complement component C1q complex binding	ITGA7	• integrin-mediated signaling pathway • cell adhesion mediated by integrin
RPE65	• phosphatidylserine binding • retinoid metabolic process	NCX1	• calcium:sodium antiporter activity • calcium ion binding • regulation of the force of heart contraction
RPL27A	• structural constituent of ribosome cytoplasmic translation	ROBO1	• Roundabout signaling pathway • aorta development
RPL4	• structural constituent of ribosome cytoplasmic translation	RRP9	• RNA binding • rRNA processing
RPS25	• structural constituent of ribosome cytoplasmic translation		
TOMM40	• protein transmembrane transporter activity • protein targeting to mitochondrion • mitochondrial outer membrane translocase complex		
VMP1	• autophagosome membrane docking • plasma membrane phospholipid scrambling • lipoprotein transport		

Table 1

970

971

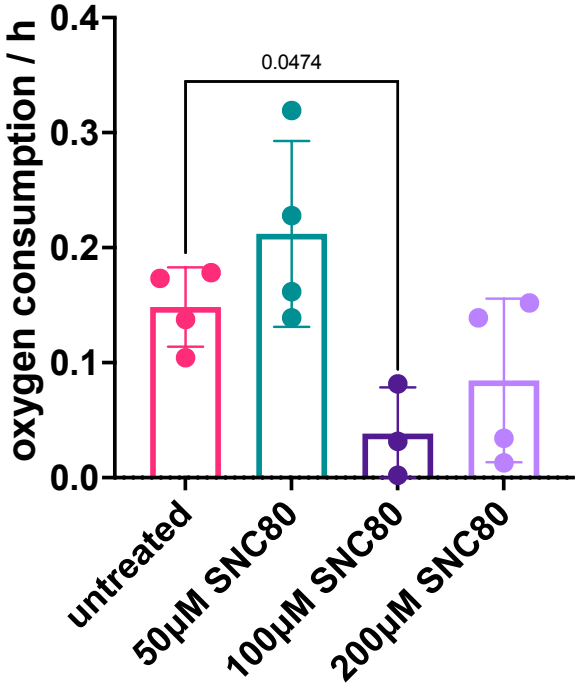

Supp. Figure S1

972
973

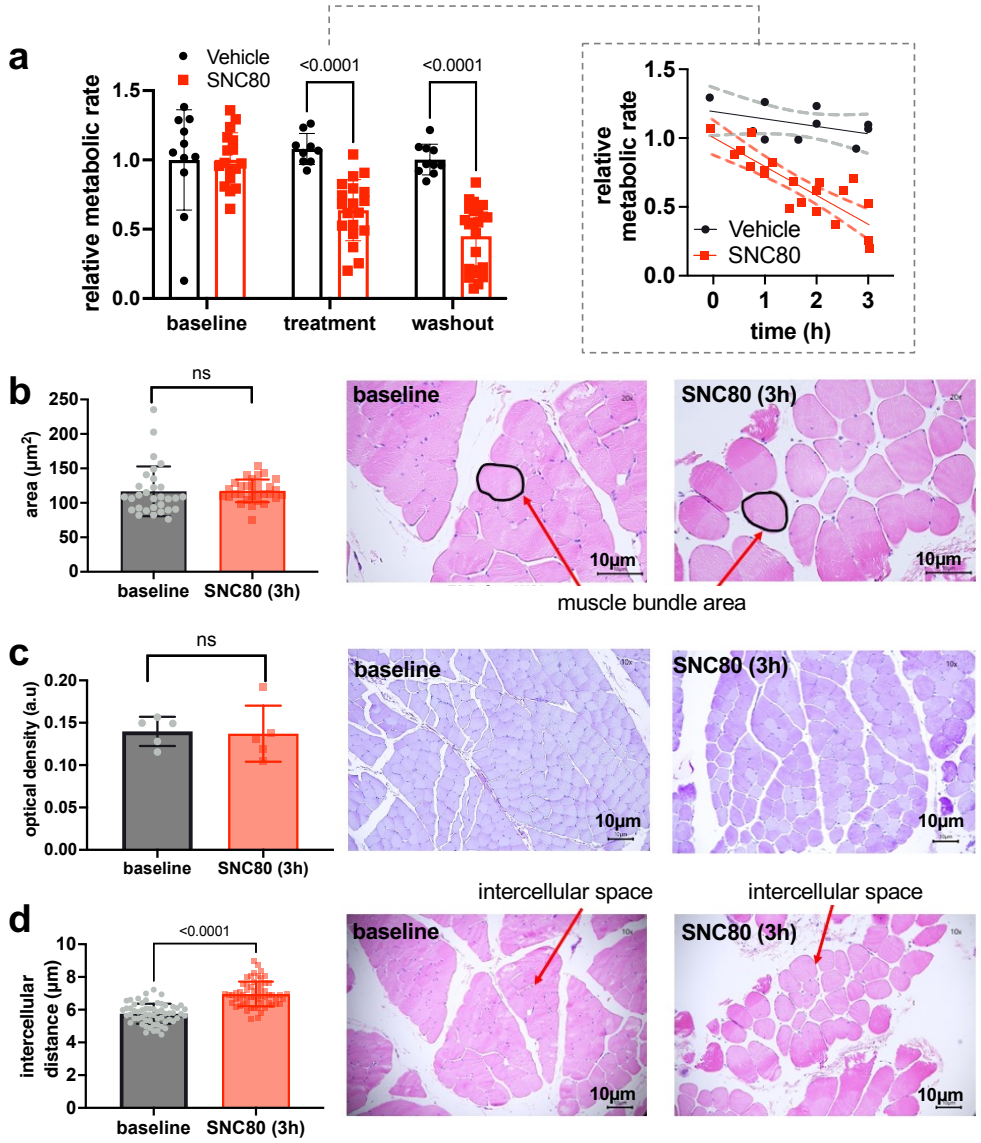

Supp. Figure S2

974

975

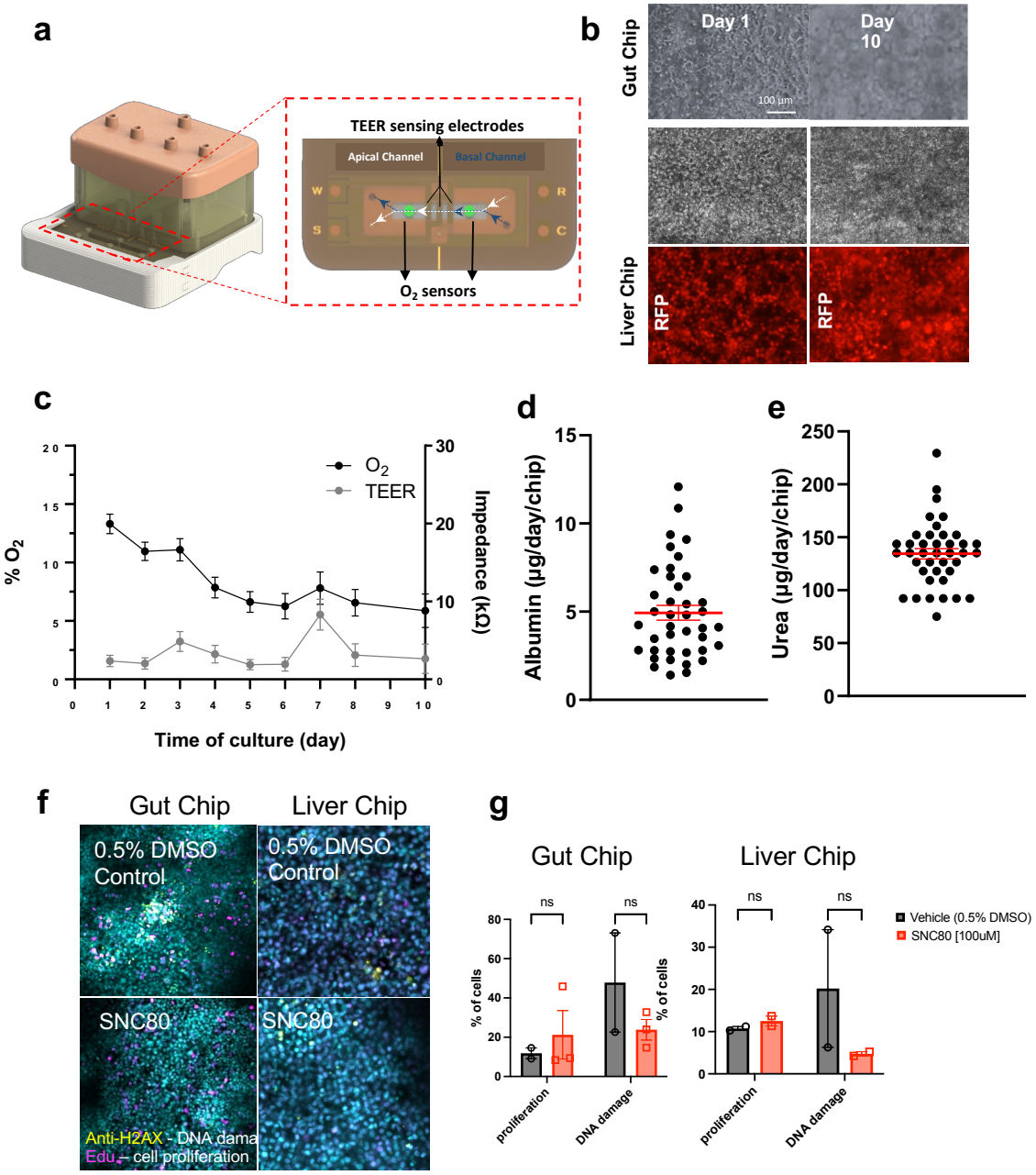

Supp. Figure S3

976

977

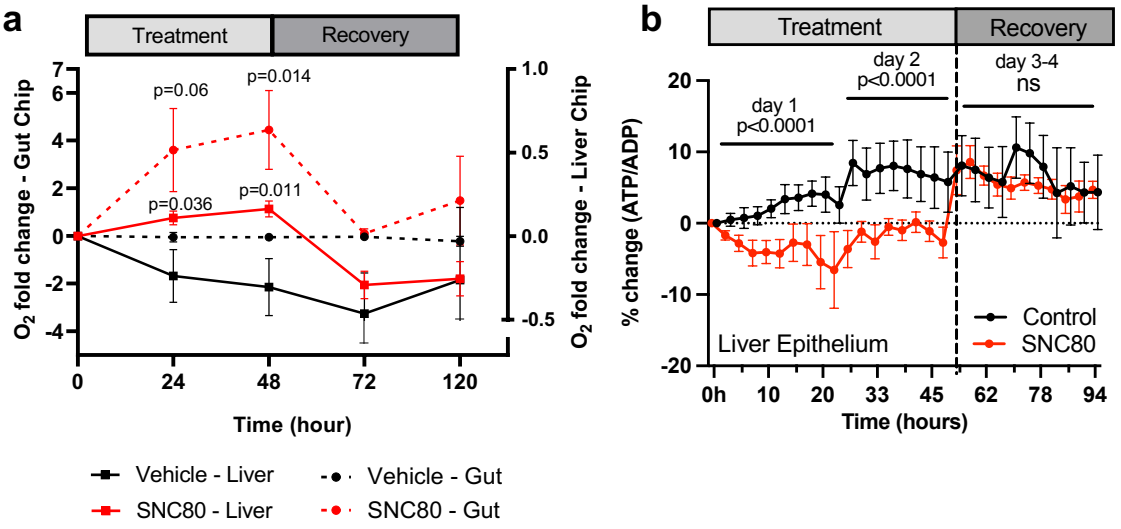

Supp. Figure S4

978

979

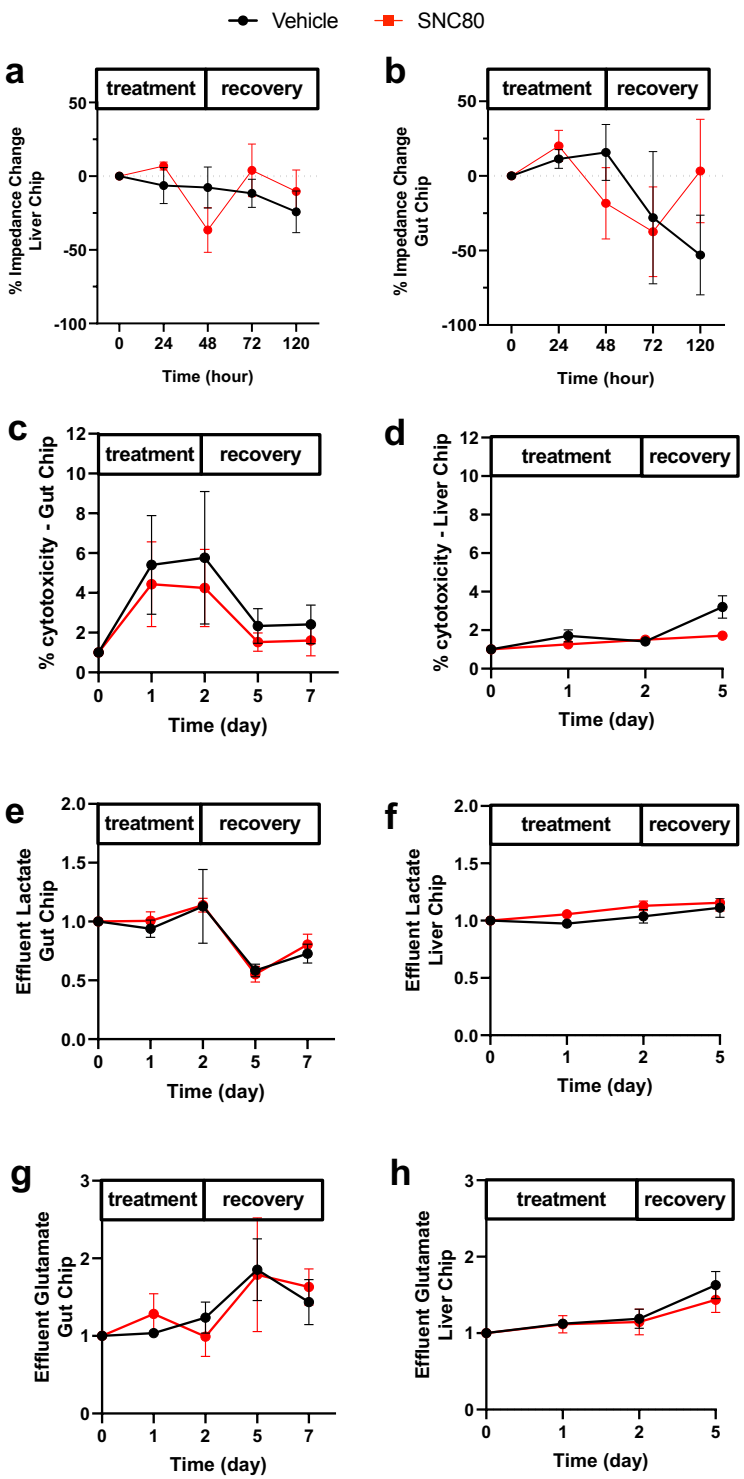

Supp. Figure S5

980

981

		Before recirculating					
		Pulse (bpm)	**Rate**	**Rhythm**	**P waves**	**QRS waves**	**T waves**
SNC80	P014	n/a	normocardic	irregular	no	no	n/a
	P015	n/a	tachycardic	irregular	no	no	n/a
	P019	n/a	n/a	n/a	n/a	n/a	n/a
	P023	12 bpm	bradycardic	irrregular	no	no	n/a
Vehicle	P016	n/a	tachycardic	irregular	no	no	n/a
	P020	n/a	tachycardic	irregular	no	no	n/a
	P024	n/a	tachycardia	irregular	no	no	n/a

		After defibrilation					
		Pulse (bpm)	**Rate**	**Rhythm**	**P waves**	**QRS waves**	**T waves**
SNC80	P014	132 bpm	tachycardic	regular	yes	yes	T wave elevation
	P015	96bpm	normocardic	irregular	yes	yes	Normal T waves
	P019	54 bpm	bradycardic	irregular	some	yes	Inconsistent T wave depression
	P023	96 bpm	normocardic	regular	no	no	Unable to assess (supraventricular tachycardia)
Vehicle	P016	144 bpm	tachycardic	regular	yes	yes	Slightly abnormal ST segment depression
	P020	132 bpm	tachycardic	regular	no	yes	T wave depression
	P024	138 bpm	tachycardic	regular	some	yes	T wave abnormal (P and T wave overlap)

Supp. Table S1

Supplemental Synthesis Description

<u>Step 1</u>: Synthesis of intermediate *N,N*-diethyl-4-formylbenzamide

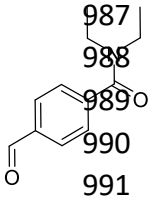

4-formylbenzoic acid (10 g, 66.61 mmol) and HATU (30.39 g, 79.93 mmol) were dissolved in DMF (500 mL) at 15 °C under N_2. The mixture was then warmed to 30 °C and stirred for 1 h. At this juncture, the mixture was cooled to 15 °C and DIEA (34.43 g, 266.43 mmol, 46.41 mL) and diethylamine (7.31 g, 99.91 mmol, 10.29 mL) were added dropwise together. The reaction was allowed to warm to rt and stirred for 12 h. The reaction mixture was diluted with H_2O (2000 mL), and then extracted with ethyl acetate (5000 mL x 3). The combined organic layers were washed with brine (1000 mL), dried over Na_2SO_4, filtered, and concentrated under reduced pressure to give a residue. The residue was purified by column chromatography (SiO_2, Petroleum ether/Ethyl acetate = 3/1 to 1/1) to give *N,N*-diethyl-4-formylbenzamide (57 g, 277.71 mmol, 83.38% yield) as a yellow solid. LC-MS m/z = 206.1 $[M+H]^+$.

<u>Step 2</u>: Synthesis of intermediate *N,N*-diethyl-4-[hydroxy(3-methoxyphenyl)methyl]benzamide

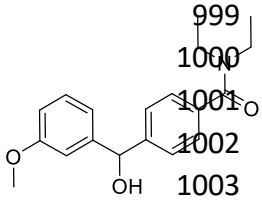

To a solution of *N,N*-diethyl-4-formylbenzamide (8 g, 38.98 mmol) in THF (320 mL) was dropwise added bromo-(3-methoxyphenyl)magnesium (1 M, 46.77 mL) at 0 °C under N_2. The reaction was stirred at 20 °C for 2 h, at which time it was diluted with H_2O (1000 mL), and then extracted with dichloromethane (500 mL x 3). The combined organic layers were washed with brine (300 mL), dried over Na_2SO_4, filtered, and concentrated under reduced pressure to give a residue. The residue was purified by column chromatography (SiO_2, Petroleum ether/Ethyl acetate = 3/1 to 1/1) to give *N,N*-diethyl-4-[hydroxy-(3-methoxyphenyl)methyl]benzamide (6 g, 19.15 mmol, 6.14% yield) as a white solid. LC-MS m/z = 314.1 $[M+H]^+$.

<u>Step 3:</u> Synthesis of intermediate 4-(chloro(3-methoxyphenyl)methyl)-*N,N*-diethylbenzamide

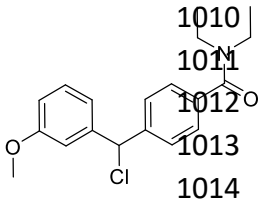

To a solution of *N,N*-diethyl-4-[hydroxy-(3-methoxyphenyl)methyl]benzamide (11.75 g, 37.49 mmol) in $CHCl_3$ (110 mL) was added dropwise HCl (12 M, 421.80 mL). The resulting mixture was stirred at 20 °C for 12 h, at which time it was diluted with H_2O (50 mL), and then extracted with dichloromethane (30 mL x 3). The combined organic layers were washed with brine (30 mL), dried over Na_2SO_4, filtered, and concentrated under reduced pressure to give 4-[chloro-(3-methoxyphenyl)methyl]-*N,N*-diethyl-benzamide (23 g, 69.31 mmol, 92.43% yield) as a yellow oil.

<u>Step 4:</u> Synthesis of WB3

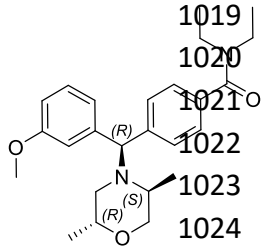

To a mixture of 4-[chloro-(3-methoxyphenyl)methyl]-*N,N*-diethyl-benzamide (23 g, 69.31 mmol) and (*2R,5S*)-2,5-dimethylmorpholine (15.97 g, 138.62 mmol) in ACN (230 mL) was added K_2CO_3 (19.16 g, 138.62 mmol). The resulting mixture was stirred at 80 °C for 4 days. The reaction mixture was filtered, and the mother liquor was directly concentrated. The residue was purified by column chromatography (SiO_2, Petroleum ether/Ethyl acetate = 5/1 to 2/1). The residue was further purified by preparative-HPLC (column: UniSil 10-120 C18 70x250mm; mobile phase: [water(FA)-ACN]; gradient:20%-50% B over 20 min) and the appropriate fractions were lyophilized. The residue was again further purified by preparative-HPLC (column: Phenomenex luna C18 (250*70mm,10 um); mobile phase: [water (FA)-ACN]; gradient:10%-50% B over 35 min) and the appropriate fractions were lyophilized to give WB3 (3.3 g, 8.03 mmol, 11.59% yield) as a white solid. LC-MS m/z = 296.1 $[M+H]^+$.

^{1}H NMR (400 MHz, $CDCl_3$) δ = 7.47 (d, J = 7.8 Hz, 2H), 7.34 - 7.27 (m, 3H), 6.88 (dd, *J* = 2.0, 8.3 Hz, 1H), 6.75 (d, *J* = 7.6 Hz, 1H), 6.72 - 6.67 (m, 1H), 5.32 (s, 1H), 3.81 (s, 3H), 3.76 - 3.66 (m, 2H), 3.64 - 3.45 (m, 2H), 3.44 - 3.24 (m, 3H), 2.61 (dd, *J* = 2.0, 11.6 Hz, 1H), 2.57 - 2.48 (m, 1H), 1.82 (dd, *J* = 9.5, 11.6 Hz, 1H), 1.24 (br d, *J* = 0.8 Hz, 3H), 1.12 (d, *J* = 6.1 Hz, 6H), 1.06 (d, *J* = 6.3 Hz, 3H).